JOURNAL OF PETROLOGY | VOLUME 40 | NUMBER 3 | PAGES 381–411 | 1999

The 15 June 1991 Eruption of Mount Pinatubo. I. Phase Equilibria and Pre-eruption P–T–$f\mathrm{O_2}$–$f\mathrm{H_2O}$ Conditions of the Dacite Magma

BRUNO SCAILLET[1]* AND BERNARD W. EVANS[2]

[1]CRSCM–CNRS, 1A RUE DE LA FÉROLLERIE, 45071, ORLÉANS CEDEX 2, FRANCE

[2]DEPARTMENT OF GEOLOGICAL SCIENCES, BOX 351310, UNIVERSITY OF WASHINGTON, SEATTLE, WA 98195-1310, USA

RECEIVED AUGUST 15, 1997; REVISED TYPESCRIPT ACCEPTED JULY 29, 1998

Crystallization experiments were carried out on a representative sample of the crystal-rich dacite ejected during the 15 June 1991 eruption of Mt Pinatubo, to define the pre-eruption conditions of this major volcanic event. Experiments were performed in the temperature and pressure range of 750–900°C and 220–390 MPa, respectively. Redox conditions were varied between those of the NNO (nickel–nickel oxide) buffer and 2·7 log $\mathrm{fO_2}$ *units above (NNO + 2·7). Melt water contents ranged from 3 to 7 wt % (H_2O saturation). Phase equilibria at 220 MPa reproduce the phase assemblage of the magma only at temperatures below 780°C and water-rich conditions: melt H_2O content > 6 wt %, or $XH_2O_{fluid} > 0{\cdot}80$. Phase abundances and the compositions of hornblende, plagioclase, and melt indicate that the eruption tapped a magma body that was at a temperature of 760 ± 20°C and a pressure in the range 220–180 MPa, with melt H_2O contents between 6 and 6·5 wt %, that is, $XH_2O_{fluid} > 0{\cdot}88$. Thermodynamic calculations constrain CO_2 in the melt to be <100 ppm. Comparison between natural and experimental Fe–Ti oxide compositions indicates that* $\mathrm{fO_2}$ *was in the range NNO + 1·5 to NNO + 1·7. Current calibrations of the Fe–Ti oxide thermobarometer are not appropriate for oxidizing conditions, and overestimate both* T *and* $\mathrm{fO_2}$ *when* $\mathrm{fO_2}$ *is greater than NNO + 1·5. Compositional zoning of plagioclase reflects crystallization over 150°C (900–750°C), and implies conditions close to, or at, H_2O saturation throughout crystallization in the upper-crustal magma chamber. Although continuous magma replenishment probably occurred, the injected magma must have had the same bulk composition (including the same melt H_2O content) as the erupted dacite to preserve the linear relationship observed between the An and Or contents of the plagioclase. Compositional zoning of hornblende is consistent either with an early crystallization event at ~400 MPa and 840–900°C, or with mixing events before eruption. The experiments show that addition of S leads to an increase in the* mg*-number of hornblende in the redox range where pyrrhotite occurs (≤ NNO + 1·4) The lack of Mg-rich overgrowth on hornblende shows that if sulfur was introduced into the magma in the course of its crystallization, such as by volatile infiltration from an underlying, triggering basalt magma, then it must have occurred when the dacite was already oxidized.*

KEY WORDS: *Pinatubo; sulfur; arc-magmas;* $f\mathrm{O_2}$; water

INTRODUCTION

The enormous amount of SO_2 (20 Mt) ejected in the 15 June 1991 eruption of Mount Pinatubo and the ensuing climatic effects (Bluth *et al.*, 1992; Hansen *et al.*, 1992, 1996) have re-emphasized the importance of S-bearing phase relations in arc magmas. The Pinatubo volcano ejected between 6000 and 10 000 Mt of dacite magma in a Plinian eruption of 9 h duration (Pallister *et al.*, 1996). The presence in the ejecta of magmatic anhydrite (Bernard *et al.*, 1991), together with hornblende, cummingtonite and biotite, indicates that both sulfur and H_2O were important volatiles in the magma chamber.

*Corresponding author. Telephone: 33 2 38 25 53 40. Fax: 33 2 38 63 64 88. e-mail: bscaille@cnrs-orleans.fr

The rock record of the role of sulfur in past eruptions is poor, however, because anhydrite does not survive more than a few years when exposed to surface waters (Arculus *et al.*, 1983; Luhr *et al.*, 1984; Luhr, 1991). Measuring the sulfur content of magmas via matrix and trapped inclusions of glass has been shown in some cases to greatly underestimate the true SO_2 output of volcanic eruptions (Devine *et al.*, 1984; Luhr, 1990; Westrich & Gerlach, 1992; Gerlach *et al.*, 1994, 1996). In most recent SO_2-producing eruptions, it has been argued that the amount of SO_2 injected into the stratosphere was not due solely to sulfur exsolution during magma ascent (Westrich & Gerlach, 1992). This is particularly true for the Pinatubo dacite magma in which the sulfur contents of undegassed melt (trapped melt inclusions) and of degassed melt (matrix glass) are virtually identical (Westrich & Gerlach, 1992; Gerlach *et al.*, 1996). To account for this excess sulfur, several explanations have been proposed: the coexistence of a sulfur and H_2O-bearing vapor phase in the magma chamber (Gerlach *et al.*, 1996), the breakdown of anhydrite following magma decompression (Baker & Rutherford, 1992), and the mixing of basalt and dacite magmas (Kress, 1997).

CURRENT CONSTRAINTS ON PRE-ERUPTION CONDITIONS

Critical in an evaluation of these hypotheses is knowledge of pre-eruption conditions, as volatile solubilities in silicate melts depend strongly, among other variables, on P, T and fO_2. Geophysical, petrological and experimental studies have defined a magma chamber at 200–300 MPa or 6–11 km depth (Pallister *et al.*, 1996; Rutherford & Devine, 1996), 780–900°C and an oxygen fugacity ~2·5–3 log units above the Ni–NiO (NNO) solid buffer (Hattori, 1993, 1996; Imai *et al.*, 1993; Matthews *et al.*, 1994; Luhr & Melson, 1996; Pallister *et al.*, 1996; Rutherford & Devine, 1996). These estimates vary considerably in their reliability, however. As stressed by Rutherford & Devine (1996), the full assemblage required for the Al-in-hornblende barometer is not present in the Pinatubo dacite (no alkali feldspar). Similarly, pressures obtained from the content of volatiles dissolved in trapped melt inclusions cannot stand alone for barometric purposes because they are known to be particularly prone to late-stage re-equilibration processes [see Pasteris *et al.* (1996)]. This means that the petrologic constraints on pressure need confirmation. For T and fO_2, the most serious limitation is that, as pointed out by Rutherford & Devine (1996), the Fe–Ti oxide thermobarometer is being used outside its calibration range, notwithstanding the empirical correction for temperature suggested by those workers. The fO_2 obtained from the composition of cummingtonite (*mg*-number = 0·71, Evans & Ghiorso, 1995) is lower by ~1·2 log units relative to that obtained from the oxides (Hattori, 1993, 1996; Pallister *et al.*, 1996; Rutherford & Devine, 1996). This disagreement was initially taken to be indicative of disequilibrium among the phenocryst minerals, but our study shows that there is no fundamental disagreement and that it is the calibration of the thermobarometer at high fO_2 that needs further work (Evans & Scaillet, 1997). A correct assessment of the redox state of the Pinatubo dacite magma is an important issue for two main reasons. First, fO_2 strongly influences both fluid speciation (Holloway, 1987) and sulfur solubilities in silicate melts (Carroll & Rutherford, 1987, 1988; Luhr, 1990), which means that uncertainty in both T and fO_2 can seriously limit our understanding of the origin of sulfur in such magmas. Second, the unusually oxidized character of the Pinatubo dacite, if really the case, emphasizes the problem of the origin of highly oxidized arc-magmas. Does it reflect an oxidized source (Carmichael, 1991) or, alternatively, is it acquired late in the evolution of the magma, for instance, by interaction with basalt-derived fluids as proposed by Hattori (1993)?

Our study was designed to find additional experimental constraints on the pre-eruption conditions of the dacite erupted at Mount Pinatubo; it emphasizes the role of sulfur in subduction zone magmas, and builds upon previous petrographical and experimental work on Pinatubo and other S-bearing arc magmas. Our experimental approach benefits from several factors. First, the multiply saturated nature of the Pinatubo dacite (coexistence of 11 phases: plagioclase–quartz–hornblende – biotite – apatite – magnetite – ilmenite – anhydrite – melt–fluid–pyrrhotite), makes this natural rock a particularly suitable subject for a phase-equilibrium approach. The stability field of this assemblage is fairly limited, and its experimental determination should provide robust constraints on the pre-eruption conditions of P, T, fO_2, fH_2O and fS_2. Second, the two main phenocryst phases in the Pinatubo dacite, plagioclase and hornblende, display significant compositional zoning, which provides additional petrogenetic information. Third, the eruptive products at Pinatubo have been studied in great detail in the last 6 years using a variety of techniques and approaches, so we already possess a highly constrained geologic framework. The procedure followed here differs from the experimental work already carried out on the Pinatubo dacite by Rutherford & Devine (1996) by providing more information on the variation of mineral compositions with intensive factors, which assists in the tightening of estimates of pre-eruption conditions. In addition, the larger T–aH_2O range explored here gives us an opportunity to trace back to earlier stages in the magmatic evolution of the dacite magma. In Part I, we present a general phase-equilibrium study of a representative 15 June dacite sample in which

the effects caused by variations in P, T and fO_2, as well as some of those related to sulfur, are used to constrain the immediate pre-eruption conditions and part of the early magmatic history. In Part II, these refined estimates of pre-eruption conditions will be used as the basis for experiments in which the sulfur content of the system is the sole experimental variable, in an effort to understand both the effect and role of sulfur in subduction-related calc-alkaline magmas of intermediate to silicic composition.

EXPERIMENTAL AND ANALYTICAL TECHNIQUES

Choice of experimental conditions and general experimental strategy

The choice of experimental conditions was guided by the results of previous investigations which indicated that the most likely pressure and temperature conditions for the top of the magma chamber were 200–300 MPa and 780–850°C. Accordingly, experiments were performed on the dacite between 200 and 400 MPa and between 760 and 900°C. The choice of fO_2 was more problematic. Although it is clear that relatively high fO_2 conditions accompanied the latest stage of crystallization of the phenocrysts, there have been suggestions of an early reduced stage in the magmatic history of the dacite (Hattori, 1993). Therefore, fO_2 was varied from NNO up to NNO + 2·7, with most of the experiments being carried out between NNO + 1 and NNO + 2.

In contrast to the experimental study of Rutherford & Devine (1996), the runs reported here are mostly crystallization experiments. Owing to the very slow cationic intracrystalline diffusion in most rock-forming minerals at temperatures below 900°C, particularly plagioclase, attainment of full chemical equilibrium when partly crystallized starting material is used requires excessively long run durations, ideally several years; in runs of a few weeks, only local equilibrium is attained, such as between the rims of the pre-existing crystals and the adjacent residual glass. This largely exludes the use of mineral compositions to retrieve petrogenetic information, especially when the original mineral is chemically zoned, as was the case for hornblende and plagioclase in the study of Rutherford & Devine (1996). To overcome this limitation, we performed crystallization experiments using dry powdered glasses of fused Pinatubo dacite together with water ($\pm$ CO_2), taken directly to the final experimental conditions (i.e. without high-temperature annealing). This procedure has recently been used in both synthetic and natural granitic systems at temperatures below 800°C with results indicative of chemical and textural bulk equilibrium (Pichavant, 1987; Holtz *et al.*, 1992; Scaillet *et al.*, 1995). Our less silicic bulk composition and the overall higher temperatures suggested that such a procedure should work equally well for the Pinatubo dacite (see also Conrad *et al.*, 1988; Martel *et al.*, 1998).

Starting products, preparation of charges

Most of the experiments were performed on a natural dacite sample kindly supplied by R. S. Punongbayan of the PHIVOLCS institute. This sample is a crystal-rich white pumice representative of the volumetrically dominant (~85%) type of ejecta produced during the climactic eruption in June 1991. It contained plagioclase (with inclusions of anhydrite, biotite and quartz), hornblende with cummingtonite overgrowth, ilmenite, magnetite, biotite, quartz, and anhydrite, in a matrix of glass. The dry glass used for crystallization experiments was prepared by twice fusing (grinding in between) ~1 g of crushed natural dacite in Pt capsules at 1400°C, 0·1 MPa for 3–4 h. During the first melting the capsule was only partially welded so as to evacuate any volatiles present, whereas for the second step of melting the capsule was welded shut. The resulting glass was finely ground under acetone to 20 μm in an agate mortar. Electron microprobe analyses showed this glass to be homogeneous within analytical uncertainty, with a bulk composition similar to those reported in the literature for the crystal-rich variety of the Pinatubo pumice (Table 1). The analytical total close to 100% suggests that this glass contains less than ~0·5 wt % H_2O. In addition, the sulfur content is below the detection limit of the electron microprobe (50 ppm), which indicates that most of the sulfur in the sample was lost during the melting. Some experiments were performed using the unfused dacite (melting experiments) crushed to a grain size of 100–200 μm. To characterize the low temperature range explored in this study, a few experiments were performed with a synthetic dry glass with a composition matching the average matrix (rhyolite) glass composition as given in published analyses (Table 1). This composition was prepared using a classical gel method (e.g. Pichavant, 1987), taking into account all major elements except P_2O_5 and MnO. The gel was then melted twice as for the dacite, to obtain a dry glass whose composition is listed in Table 1.

Charges were loaded into Au capsules of 15 mm length, 2·5 mm internal diameter and 0·2 mm wall thickness. Deionized H_2O, CO_2 (as silver oxalate) and the silicate were added as described by Scaillet *et al.* (1995), except that fluid/silicate weight ratios were maintained in the range 1/9 to 1·5/8·5. Elemental sulfur was added to

Table 1: Starting compositions (wt %)

	Dacite[1]					Matrix glass[1]	
	Pallister *et al.*	Bernard *et al.*	Luhr & Melson	Fournelle *et al.*	This study (dry glass)	Literature	Synthetic (dry glass)
n:[2]	7	15	1	3	5	13	18
SiO_2	64·76	65·06	64·65	65·53	65·50(52)[4]	77·75(105)	78·29(49)
Al_2O_3	16·54	16·14	16·81	16·25	16·35(33)	13·11(54)	12·85(28)
FeO[3]	4·38	4·25	4·39	4·13	4·50(16)	0·95(27)	1·06(25)
MgO	2·40	2·47	2·41	2·35	2·11(9)	0·21(4)	0·20(6)
MnO	0·10	0·10	0·10	0·10	0·14(12)	—	—
CaO	5·24	5·22	5·17	4·97	4·82(27)	1·26(19)	1·31(12)
Na_2O	4·50	4·72	4·45	4·56	4·45(5)	3·65(49)	3·29(15)
K_2O	1·54	1·54	1·52	1·58	1·67(10)	2·95(15)	2·85(10)
TiO_2	0·53	0·49	0·50	0·53	0·45(3)	0·13(7)	0·15(7)
Total[5]	99·90	99·75	99·14	99·29	98·54	100·10	100·00

[1]Bulk rock and matrix glass analyses from Bernard *et al.* (1996), Fournelle *et al.* (1996), Luhr & Melson (1996) and Pallister *et al.* (1996). All analyses are normalized to 100% anhydrous.
[2]Number of analyses.
[3]Total iron as FeO.
[4]Numbers in parentheses indicate one standard deviation of replicate analyses in terms of smallest units cited.
[5]Original totals.

some charges with the aid of a high-precision Sartorius balance that allowed us to weigh amounts to $\pm 0{\cdot}001$ mg.

Experimental equipment

Experiments were performed mostly in two internally heated pressure vessels (IHPV). One, working horizontally and not equipped with an H_2 membrane, was used for temperatures below 830°C and very oxidizing conditions (>NNO + 2). The other, working vertically, and fitted with a Shaw-type membrane for the control of H_2 fugacity (fH_2), was used for higher temperatures and moderately oxidizing conditions (<NNO + 2). This vessel was also used with a fast quench device, in which case the membrane was removed because of the limited room available. Cold-seal pressure vessels (CSPV) equipped with Shaw membranes were also used at temperatures $\leq$780°C. The pressure medium was either Ar (IHPV without membrane) or a mixture of Ar + H_2 obtained by sequential loading at room temperature [IHPV with membrane; see Scaillet *et al.* (1992, 1995)] or by direct H_2 diffusion across the membrane (CSPV) under the experimental conditions (Schmidt *et al.*, 1995). Total pressure was continuously monitored by transducers calibrated against a Heise Bourdon tube gauge with an uncertainty of ~2 MPa. In the IHPV, temperatures were recorded by two or three sheathed, type K thermocouples. In the CSPV, temperatures were recorded by an external unsheathed type-K thermocouple. All thermocouples were calibrated against NaCl at 0·1 MPa. Temperature gradients in the hot-spot zones were always <3°C. The overall temperature uncertainty is $\pm$5°C [see Scaillet *et al.* (1992) and Schmidt *et al.* (1995)].

Experiments consisted of running simultaneously either 8–11 (IHPV) or two (CSPV) capsules. All but one experiment (899°C) in the IHPV were terminated by switching off the power supply, resulting in temperature decreases of about 400°C during the first 4 min. To prevent quench crystallization, the 899°C experiment was ended with a fast quench device (Roux & Lefèvre, 1992). Upon quenching the sample holder fell instantaneously into the coldest part of the vessel (~50°C), producing a total pressure increase of ~40 bars. Runs in the CSPV were ended by removing the vessel from the furnace with cooling rates similar to those of the IHPV without the fast quench device. No isobaric quench was carried out (except for the 899°C run), and total pressure dropped by about half of its initial value during cooling in the IHPV and by about 1/3 in the CSPV. A total of six temperatures was explored (747, 759, 776–785, 834, 866 and 899°C) at pressures of 220 and 390 MPa

(Table 2). Run durations varied between 162 and 470 h depending on temperature.

Control of fH_2, fH_2O, and fO_2

The redox state of the experimental charges was controlled by the fH_2 of the fluid pressure medium and, depending on the desired final fO_2, two different methods were used. For $fO_2 < NNO + 2$, except for the run at 899°C, fH_2 was continuously read with Shaw membranes connected to transducers, with an uncertainty on fH_2 of $\pm 0{\cdot}02$ MPa at a level of 0·3–0·4 MPa for run durations of 10 days. In the CSPV, variations in H_2 pressures were always <0·03 MPa [see Schmidt *et al.* (1995)]. The fH_2 read by Shaw membranes was checked against NiPd-based solid sensors (see below for details of preparation). In the IHPV the calculated fH_2 from the sensor agreed to within 0·001 MPa with the value measured by the membrane, whereas in the CSPV the calculated value differed by 0·02 MPa. For $fO_2 > NNO + 2$, we used the IHPV loaded with Ar only with an intrinsic fH_2 that generates fO_2 in the range NNO + 2 to NNO + 3 (Scaillet *et al.*, 1992). The fH_2 of these runs was measured by using the solid sensor method of Taylor *et al.* (1992), except for two runs in which the hornblende composition was used to infer the fO_2 (Table 2). The sensor consisted of hand-pressed Ni–Pd–NiO pellets loaded with distilled and deionized water into Pt capsules lined with ZrO_2 powder to prevent contamination with Pt. Sensor compositions were found to be homogeneous within analytical uncertainties (standard deviation $\pm$ 0·003 X_{Ni} for 10–20 analyses on a single sensor). After calculating the fO_2 using the formulation of Pownceby & O'Neill (1994), the fH_2 was calculated using the Lewis and Randall approximation and fugacity coefficients of Shaw & Wones (1963) for pure H_2 and Burnham *et al.* (1969) for pure H_2O, in addition to the dissociation constant of H_2O from Robie *et al.* (1979). The sensor technique was also used for the determination of the fH_2 of the run at 899°C.

All experiments were fluid saturated and water activity (aH_2O) was varied by the addition of CO_2 to the charges. Owing to the small fluid/silicate ratios used in this study, the final fluid compositions were significantly different from the starting ones because of water uptake by the silicate melt. The final equilibrium fluid composition was calculated neglecting the melt CO_2 content, knowing melt abundances from mass-balance constraints and melt H_2O content from the electron microprobe analysis (see below). For runs with added CO_2 ($aH_2O < 1$), the maximum possible fO_2 was calculated, assuming ideal mixing in the fluid phase and constant fH_2 (Whitney, 1972; Webster *et al.*, 1987), from the relation

$$\log fO_2 = \log fO_2 \text{ (at } aH_2O = 1) - 2 \log XH_2O_{in}$$

where XH_2O_{in} is the mole fraction of H_2O in the starting fluid. This fO_2 estimate is a maximum because of the systematic decrease of the XH_2O in the fluid phase relative to that of the starting fluid phase (see Table 2). For H_2O-saturated charges, the overall uncertainty on fO_2 is $\pm 0{\cdot}2$ log units.

Analytical techniques

Run products were characterized by reflected light, powder X-ray diffraction (XRD), scanning electron microscopy (SEM) and electron microprobe methods. Analytical conditions for the electron microprobe were accelerating voltage 15 kV, sample current 6 nA, counting time of 10 s on peak for all elements, and a focused beam for minerals and defocused beam for glasses (5 μm). Na and K were always analyzed first and a ZAF correction procedure was used. Alkali element migration in glass under the probe beam was assessed using established correction procedures, which involved the use of secondary hydrous glasses of known alkali contents to evaluate empirical correction factors for Na and K (Pichavant, 1987; Scaillet *et al.*, 1995). Water contents of quenched glasses were estimated with a modification of the by-difference method (e.g. Devine *et al.*, 1995), that used eight standard synthetic rhyolitic glasses (75–77 wt % SiO_2) containing between 1·9 and 8·7 wt % H_2O as determined by Karl Fischer titration or ion microprobe analyses on separate glass chips (Scaillet *et al.*, 1995; Martel, 1996).

Apart from the 899°C run (charges 42–50) and those carried out with the synthetic rhyolitic composition (charges 72–75), the glass analyzed in all charges at water-saturated conditions had H_2O contents in the range of 7–8 wt %, which is up to 1 wt % higher than previously obtained for melts of rhyolitic composition at the same experimental conditions (e.g. Silver *et al.*, 1990; Holtz *et al.*, 1995). We interpret this excess H_2O as resulting from incipient exsolution of vapour taking place during the quench, which produces micrometer-sized H_2O bubbles that decrease the probe total. This exsolution is probably enhanced in crystal-rich charges, as bubble nucleation has been shown to be facilitated by the presence of microlites in natural obsidians (Hurwitz & Navon, 1994). This explains why the near-liquidus synthetic rhyolitic glass has H_2O contents of ~7 wt % at 780°C, whereas matrix rhyolitic glass in the crystal-rich dacite under the same conditions is apparently richer in H_2O, in spite of comparable quenching rates. Accordingly, our estimates of melt H_2O were corrected by subtracting from all analyses the H_2O that in fact was void space. To do this the melt water contents for water-saturated charges obtained with the dacite bulk composition in the range

Table 2: Experimental conditions, run products and phase proportions

Run no.	Starting material	ΔNNO[1]	XH_2O_{in}[2]	XH_2O_{fin}[2]	H_2O melt[3] (wt %)	Total S (wt %)	Run products and phase proportions[4] (wt %)	Σr^2
P_t *2212 bar,* PH_2 *0·4 bar,*[5] T *785°C, run duration 470 h, IHPV*								
4	crushed rock	2·70	1·00	1·00	7·00	—	Gl, Pl, Hbl, Ilm, Mag	—
5	crushed rock	2·61	0·90	—	6·28	—	Gl, Pl, Hbl, Ilm, Mag	—
6	crushed rock	2·51	0·80	—	6·36	—	Gl, Pl, Hbl, Ilm, Mag	—
7	crushed rock	2·39	0·70	—	*5·20*	—	Gl, Pl, Hbl, Ilm, Mag, Bt	—
8	dry glass	2·70	1·00	1·00	7·00	—	Gl(57·2), Pl(28·1), Hbl(11·7), Ilm(1·0), Mag(2·0)	0·26
9	dry glass	2·61	0·90	0·86	6·69	—	Gl(47·4), Pl(37·6), Hbl(12·0), Ilm(0·9), Mag(2·0)	0·14
10	dry glass	2·51	0·80	—	*5·74*	—	Gl, Pl, Hbl, Ilm, Mag, Qtz	—
11	dry glass	2·39	0·70	—	*5·20*	—	Gl, Pl, Hbl, Ilm, Mag, Qtz	—
P_t *2238 bar,* PH_2 *8·5 bar,*[6] T *776°C, run duration 310 h, CSPV*								
16	dry glass	−0·01	1·00	1·00	7·00	—	Gl(52·3), Pl(32·5), Hbl(14·7), Ilm(0·5)	0·62
17	dry glass	−0·01	1·00	1·00	7·00	1·20	Gl(55·0), Pl(29·6), Hbl(11·9), Ilm(0·3), Po(3·3)	0·64
P_t *2238 bar,* PH_2 *2·6 bar,*[6] T *776°C, run duration 310 h, CSPV*								
18	dry glass	1·04	1·00	1·00	7·00	—	Gl(50·8), Pl(31·5), Hbl(17·0), Ilm(0·7)	0·73
19	dry glass	1·04	1·00	1·00	7·00	1·10	Gl(52·8), Pl(31·5), Hbl(12·1), Ilm(0·3), Po(3·4)	0·77
P_t *2245 bar,* PH_2 *1·2 bar,*[6] T *776°C, run duration 310 h, CSPV*								
20	dry glass	1·71	1·00	1·00	7·00	—	Gl(49·8), Pl(34·3), Hbl(13·5), Ilm(0·2), Mag(2·2)	0·05
21	dry glass	1·71	1·00	1·00	7·00	1·04	Gl(53·0), Pl(31·8), Hbl(8·0), Ilm(0·2), Mag(2·9), Anh(0·7), Bt(3·5)	0·22
P_t *2300 bar,* PH_2 *1·0 bar,*[5] T *834°C, run duration 328 h, IHPV*								
22	dry glass	2·01	1·00	1·00	7·00	—	Gl(67·4), Pl(17·7), Hbl(12·9), Mag(2·1)	0·57
23	dry glass	1·93	0·91	0·88	6·96	—	Gl(64·2), Pl(20·3), Hbl(12·9), Mag(2·6)	0·28
24	dry glass	1·82	0·80	0·74	5·76	—	Gl(56·3), Pl(29·0), Hbl(11·5), Mag(2·7), Opx(0·8), Ilm(<0·1)	0·14
25	dry glass	1·71	0·71	0·64	6·19	—	Gl(41·7), Pl(45·8), Hbl(6·0), Mag(2·2), Opx(3·9), Ilm(0·4)	0·29
26	dry glass	1·56	0·60	—	*5·00*	—	Gl, Pl, Mag, Ilm, Opx, Qtz	—
27	dry glass	1·37	0·48	—	*4·26*	—	Gl, Pl, Mag, Ilm, Opx, Qtz	—
28	dry glass	1·21	0·40	—	*3·76*	—	Gl, Pl, Mag, Ilm, Opx, Qtz	—
29	dry glass	0·96	0·30	—	*3·10*	—	Gl, Pl, Mag, Ilm, Opx, Qtz	—
30	crushed rock	2·01	1·00	1·00	7·00	—	Gl, Pl, Hbl, Mag	—
P_t *2247 bar,* PH_2 *1·1 bar,*[6] T *759°C, run duration 448 h, CSPV*								
31	dry glass	1·70	1·00	1·00	7·00	—	Gl, Pl, Hbl, Mag, Ilm	—
32	dry glass	1·61	0·90	—	*6·02*	—	Gl, Pl, Hbl, Mag, Ilm, Qtz	—
P_t *2088 bar,* PH_2 *3·1 bar,*[6] T *866°C, run duration 162 h, IHPV*								
33	dry glass	1·00	1·00	1·00	7·00	—	Gl(68·5), Pl(16·1), Hbl(13·9), Mag(1·5)	0·56
34	dry glass	0·91	0·90	0·87	6·21	—	Gl(62·3), Pl(22·7), Hbl(13·8), Mag(1·3), Opx(0·5)	0·39
35	dry glass	0·81	0·80	0·76	5·04	—	Gl(56·0), Pl(29·6), Hbl(10·0), Mag(1·4), Opx(3·2), Ilm(<0·1)	0·14
36	dry glass	0·69	0·70	0·59	6·07	—	Gl(52·6), Pl(35·9), Opx(10·4), Mag(0·6), Ilm(0·6)	0·50
37	dry glass	0·56	0·60	—	*4·74*	—	Gl, Pl, Opx, Mag, Ilm, Qtz, Cpx	—
38	dry glass	0·38	0·49	—	*4·11*	—	Gl, Pl, Opx, Mag, Ilm, Qtz, Kfs	—
39	dry glass	0·20	0·40	—	*3·57*	—	Gl, Pl, Opx, Mag, Ilm, Qtz, Cpx	—
40	dry glass	−0·05	0·30	—	*2·94*	—	Gl, Pl, Opx, Mag, Ilm, Qtz, Kfs	—
41	crushed rock	1·00	1·00	1·00	7·00	—	Gl, Pl, Hbl, Mag, Anhy	—

Table 2: continued

Run no.	Starting material	ΔNNO[1]	XH_2O_{in}[2]	XH_2O_{fin}[2]	H_2O melt[3] (wt %)	Total S (wt %)	Run products and phase proportions[4] (wt %)	Σr^2
P_t *2250 bar,* PH_2 *2·8 bar,*[7] T *899°C, run duration 191 h, IHPV*								
42	dry glass	1·20	1·00	1·00	6·96	—	Gl(87·9), Pl(3·3), Hbl(8·3), Mag(0·5)	0·03
42b	dry glass	1·20	1·00	1·00	6·24	1·0	Gl(88·5), Pl(2·9), Hbl(6·0), Anhy(0·6), Po(2·0)	0·05
43	dry glass	1·11	0·90	0·86	6·04	—	Gl(77·7), Pl(11·6), Hbl(10·1), Mag(0·6)	0·05
44	dry glass	1·01	0·80	0·73	5·66	—	Gl(71·0), Pl(18·0), Hbl(8·8), Opx(1·4), Mag(1·3), Ilm(<0·1)	0·04
45	dry glass	0·89	0·70	0·65	3·78	—	Gl(54·0), Pl(33·8), Opx(10·2), Ilm(0·7), Qtz(1·2)	0·35
46	dry glass	0·80	0·63	0·56	3·09	—	Gl(52·0), Pl(36·2), Opx(11·7), Ilm(0·6), Qtz(<0·1), Cpx(<0·1)	0·16
47	dry glass	0·56	0·48	—	*4·33*	—	Gl, Pl, Opx, Ilm, Qtz, Kfs	—
48	dry glass	0·38	0·39	—	*3·76*	—	Gl, Pl, Opx, Qtz, Ilm	—
49	dry glass	0·26	0·34	—	*3·43*	—	Gl, Pl, Opx, Qtz, Ilm	—
50	crushed rock	1·20	1·00	1·00	6·98	—	Gl, Pl, Hbl, Mag	—
P_t *2237 bar,* PH_2 *0·60 bar,*[7] T *781°C, run duration 330 h, IHPV*								
51	dry glass	2·27	1·00	1·00	7·00	—	Gl(55·3), Pl(29·0), Hbl(13·0), Mag(2·2), Ilm(0·4)	0·27
52	dry glass	2·27	1·00	1·00	7·00	0·95	Gl(58·5), Pl(27·2), Ged(10·1), Bt(0·5), Mag(2·5), Ilm(0·3), Anhy(0·9)	0·23
53	dry glass	2·17	0·89	0·85	6·50	1·02	Gl(46·2), Pl(36·8), Ged(13·1), Opx(<0·1), Mag(1·7), Ilm(1·0), Anhy(1·2)	0·39
58	dry glass	2·27	1·00	—	5·83	0·32	Gl(52·5), Pl(32·7), Hbl(10·6), Opx(<0·1), Mag(2·3), Ilm(0·5), Anhy(0·4)	0·09
P_t *3890 bar,* PH_2 *0·71 bar,*[7] T *780°C, run duration 354 h, IHPV*								
65	dry glass	2·63	1·00	1·00	8·50	—	Gl(62·0), Pl(21), Hbl(14·6), Mag(1·2), Ilm(1·1)	0·53
66	dry glass	2·54	0·90	0·86	8·08	—	Gl(51·1), Pl(31·9), Hbl(14·5), Mag(1·4), Ilm(1·1)	0·23
67	dry glass	2·44	0·80	0·74	7·27	—	Gl(46·9), Pl(36·7), Hbl(14·3), Mag(1·2), Ilm(0·9)	0·11
68	dry glass	2·33	0·71	—	–	—	Gl, Pl, Hbl, Mag, Ilm	
69	dry glass	2·63	1·00	—	8·15	1·35	Gl(73·7), Pl(11·3), Ged(1·6), Bt(7·5), Mag(2·8), Ilm(0·7), Anhy(2·4)	0·68
P_t *2174 bar,* PH_2 *1·7 bar,*[6] T *747°C, run duration 502 h, CSPV*								
72	dry glass[8]	1·30	0·89	0·80	6·38	—	Gl(95·4), Pl(4·1), Mag(0·5), Bt(<0·1)	2·67
73	dry glass	1·30	0·90	0·81	6·35	1·11	Gl(92·0), Pl(6·8), Po(1·2)	6·94
P_t *2174 bar,* PH_2 *1·7 bar,*[6] T *778°C, run duration 502 h, CSPV*								
74	dry glass[8]	1·40	1·00	1·00	7·01	—	Gl(99·6), Mag(0·4)	0·17
75	dry glass	1·40	1·00	1·00	6·90	1·12	Gl(99·1), Po(0·7), Anhy(0·2)	0·18

[1]ΔNNO = log fO_2 (experiment) – log fO_2 (NNO; Chou, 1987). For H_2O-undersaturated runs, the maximum possible fO_2 is calculated as log fO_2 = log $fO_{2(aH2O=1)}$ –2log XH_2O_{in}.
[2]XH_2O_{in} = $H_2O/(H_2O + CO_2)$ loaded in the capsule (in moles). XH_2O_{fin} is the equilibrium fluid phase composition, obtained from mass balance constraints.
[3]Numbers in italics indicate wt % H_2O in melt calculated after Silver *et al.* (1990) with $fH_2O = XH_2O_{in} \times fH_2O^{pure}$ at the experimental *P* and *T* and regular solution parameters for a rhyolitic composition.
[4]Phase proportions calculated using a constrained least-squares mass balance with propagation of analytical errors of the experimental phases (Albarède, 1995). Standard deviations for phase abundances are <3% for a wt % phase >50, <5% for wt % phase 20–50, <10% for wt % phase 2–20, and >10% for wt % phase <2.
[5]fH_2 obtained with fO_2 calculated from the *mg*-number of hornblende crystallized at $aH_2O = 1$ (see Table 4) and the polynomial fit of Fig. 5, after correction for the temperature effect on *mg*-number.
[6]fH_2 from membrane reading in internally heated pressure vessel (IHPV) or in cold-seal pressure vessel (CSPV).
[7]fH_2 from NiPd sensor measurement.
[8]Synthetic rhyolitic glass of Table 1 used as starting material.
Phase abbreviations: Gl, glass; Pl, plagioclase; Hbl, hornblende; Opx, orthopyroxene; Cpx, clinopyroxene; Ged, gedrite; Mag, magnetite; Ilm, ilmenite; Bt, biotite; Qz, quartz; Kfs, alkali feldspar; Anhy, anhydrite; Po, pyrrhotite.

780–866°C at 220 MPa were all set to a constant value of 7 wt % H_2O, and the excess 'H_2O' was subtracted from the measured values in the runs at the same temperature but lower aH_2O. The two most crystallized samples analyzed at 834°C (charge 25, Table 2) and 866°C (charge 36, Table 2) gave H_2O contents that are too high relative to neighboring charges. These two charges were not used to draw the T°C–melt H_2O content diagram shown in Fig. 2a (below). Apart from these two charges, we believe that water contents obtained with this method are accurate to 1 wt % absolute, and differences in H_2O content of more than 0·4 wt % between samples analyzed during the same analytical session are considered to be real.

RESULTS

General observations

Our crystallization experiments produced textural features similar to those observed in crystallization experiments carried out in natural granitic systems (e.g. Scaillet *et al.*, 1995). These features include: (1) homogeneous distribution of all phases present (glass + crystals + bubbles); (2) homogeneity of crystal sizes and euhedral shapes; (3) bubble sizes that were homogeneous in CO_2-free experiments but more variable in CO_2-bearing ones. Below 830°C crystal sizes rarely exceeded 10 μm (Fig. 1), whereas above this temperature lengths of 20 μm are more common. Crystalline phases identified in run products were plagioclase, hornblende, orthopyroxene, clinopyroxene, quartz, magnetite, and ilmenite. In sulfur-bearing experiments additional phases present were biotite, anthophyllite, gedrite, pyrrhotite, and anhydrite, the appearance of the last two phases depending on the prevailing fO_2. Therefore, apart from cummingtonite, crystallization experiments were successful in reproducing the natural phase assemblage.

Textures observed in the few melting experiments contrast sharply with those of their crystallizing counterparts, yet, with the exception of biotite (see Table 2), the phase assemblages obtained were similar. The major difference is the apparently larger amount of residual liquid obtained in melting experiments, probably an artifact of the larger crystal sizes, which increase the size of residual liquid pools. The larger crystals (>50 μm) are mostly angular fragments, whereas the small ones are euhedral, suggesting that they grew during the experiment. At 866°C, needle-like phases were observed to grow on the edges of the relict crystals present in the melting experiment, most of them in a star-like display. Although we could not identify these phases, we interpret these textures as resulting from quench crystallization. This was the main reason for using the fast quench device at 899°C.

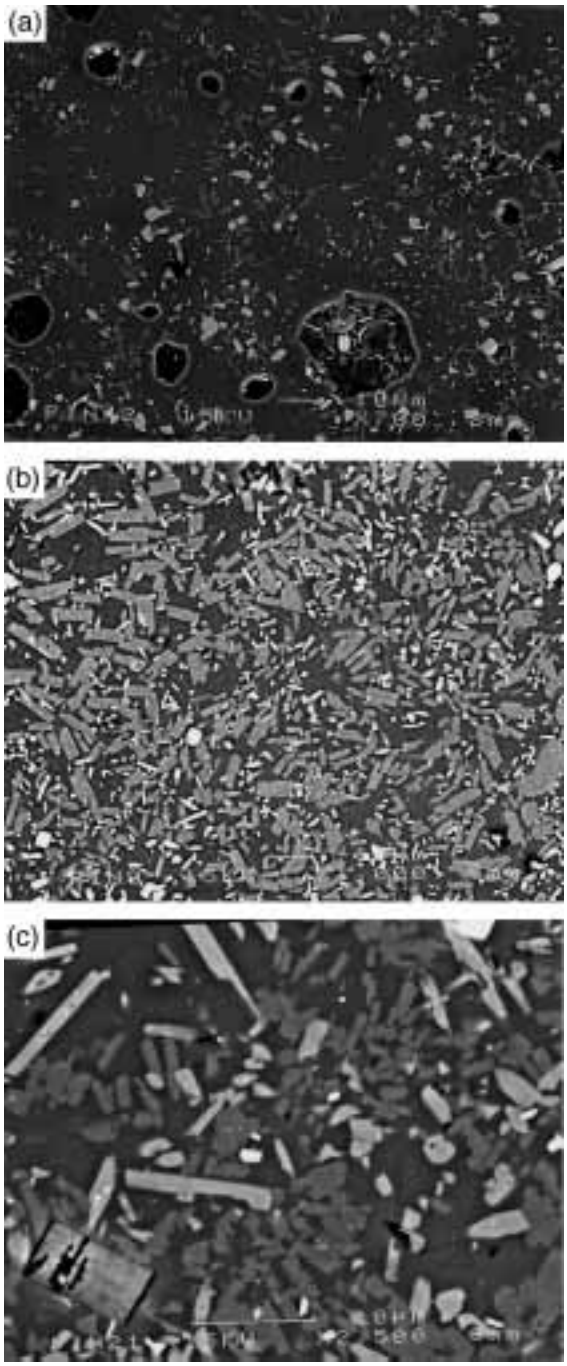

Fig. 1. Scanning electron microscope images of selected run products obtained in crystallization experiments at (a) 899°C and H_2O-saturated conditions (charge 42), and (b) and (c), 780°C and H_2O-saturated conditions (charges 8 and 21). In (a) plagioclase is gray and lath-like, hornblende is pale gray and subequant, magnetite is small, bright and squarish, and glass is dark gray. In (b) abundant plagioclase (rectangular gray crystals) coexists with small prisms of hornblende (bright elongated crystals) and Fe–Ti oxides (magnetite and ilmenite, equant bright phases, especially in the middle of the upper border). In (c) plagioclase, hornblende and Fe–Ti oxides (upper right corner) coexist with a euhedral crystal of anhydrite (lower left) and glass. [Note the different scales between (b) and (c).]

From the viewpoint of phase petrology, crystallization experiments gave results consistent with an overall close approach to bulk equilibrium. The compositions of product phases are homogeneous in a given charge, except for plagioclase in some charges (see below). Solid-solution phases display continuous and smooth compositional changes with variations in the main intensive variables T, aH_2O and fO_2. Similarly, the product liquid composition is homogeneous throughout a given experimental charge. In contrast, crystal compositions in melting experiments show significant chemical heterogeneity that in most cases could not be simply related to the position of the analysis relative to the outer boundaries of the analyzed mineral (plagioclase, hornblende). Much of this chemical variability matches that in the natural rock, showing that in large measure heterogeneity is inherited from the original zoning. Nevertheless, several features suggest that local crystal–melt equilibrium was attained in many cases. First, neocrystallization on the edges of the relict plagioclase is common, although unevenly distributed. Second, Fe–Ti oxides display an outer ~20 μm (or more) re-equilibrated rim, suggesting fast cationic diffusion in the crystals, with convergence of rim compositions to those in the crystallization experiments. Third, glasses are homogeneous within analytical uncertainty and their compositional variations are closely correlated with changes in the experimental variables. In addition, the chemical trends observed are comparable with those obtained in crystallization experiments, especially when the experimental conditions were close to those under which the magma last equilibrated (i.e. pre-eruption conditions). The only major exception to this general approach to local equilibrium is the hornblende. Scanning electron microscope images reveal that the largest crystals display complex zoning patterns with no evidence of incipient re-equilibration even at their outer rims; hornblende is clearly poorly to non-reactive in melting experiments under the experimental conditions used. Overall, it appears that the closer the experimental conditions are to the pre-eruptive conditions in melting experiments, the better is the agreement between melting and crystallization experiments. The crystallization experiments have contributed to a clearer understanding of the results of the melting experiments.

Phase identification

A combination of reflected light microscopy, XRD, SEM and electron microprobe analysis was used for phase identification. The presence of clinopyroxene was inferred from the high CaO content (>15 wt %) of some microprobe analyses of Fe–Mg silicates obtained in certain high-temperature and low-H_2O charges (Table 2). Similarly, the presence of alkali feldspar was inferred from the high K_2O content of feldspar analyses (>3–4 wt %). Despite extensive search, cummingtonite was not detected in any of the crystallization experiments. Scanning electron microscope images of run products obtained in melting experiments at 780°C failed to show any cummingtonite rims left over on relict hornblende crystals. Clearly, cummingtonite in trace amounts may have been overlooked. However, identification of biotite (in sulfur-bearing runs) was not a problem at levels of 1–2%. Anthophyllite and gedrite were readily detected in sulfur-bearing runs. For these reasons, we believe that cummingtonite was not a run product in any of our sulfur-free runs. Experimental data reported here, and in expanded form in Part II, suggest that the crystallization of ferromagnesian amphibole is related to the sulfur content of the sample and the resulting uptake of Ca by anhydrite. Finally, anhydrite and pyrrhotite were confirmed by electron microprobe only. Anhydrite displays rectangular shapes with sizes slightly larger than the other crystals (Fig. 1), whereas pyrrhotite displays mostly rounded shapes.

Phase relations

Details of experimental run conditions and product assemblages are listed in Table 2. Phase boundaries (Fig. 2) are drawn based on crystallization experiments only, in which fO_2 ranged from NNO to NNO + 2·7; a consistent picture emerges despite this range in fO_2. Some results from sulfur-bearing experiments (up to 1 wt % S) were used as well because the addition of elemental sulfur influences the stability of some phases (biotite, Fe–Mg amphibole, orthopyroxene) even at low concentration levels (see Part II). Two graphical representations of direct petrologic use are presented in Fig. 2: T–wt % H_2O–melt, and T–XH_2O_{fluid}. Because these phase diagrams critically depend on our capacity to analyze the run products, especially the melt phase, the number of data used in their construction is smaller than the full experimental data set. For the H_2O-poor region of the T–wt % H_2O–melt diagram (Fig. 2a), an approximate H_2O–melt value for the charges in which the melt could not be analyzed was obtained by using the water solubility model of Silver *et al.* (1990). The fH_2O of those runs was calculated assuming ideal mixing in the fluid phase and using the initial fluid phase composition:

$$fH_2O = XH_2O_{in} f°H_2O$$

where $f°H_2O$ is the fugacity of pure H_2O at the experimental P and T (Burnham *et al.*, 1969). Given that XH_2O_{in} is a maximum for XH_2O in the coexisting fluid, melt H_2O contents derived in this way are also maximum values (Table 2, Fig. 2a). They are nevertheless useful for constraining the water-poor region of the phase

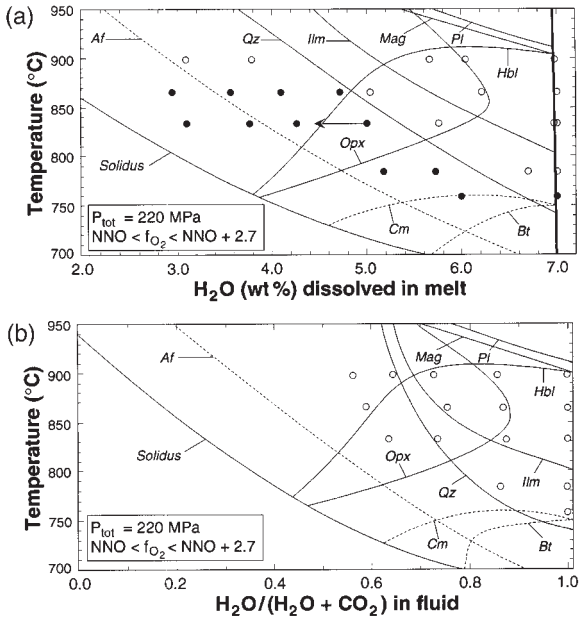

Fig. 2. Isobaric phase relations of the crystal-rich Pinatubo dacite at 220 MPa as a function of (a) melt H_2O content and (b) XH_2O of the coexisting fluid phase. Curves are labelled with mineral names lying inside their stability fields. ○, charges for which the melt H_2O content was determined using the by-difference method; ●, those where the melt H_2O content was calculated as explained in the text. Charges 25 and 36 are not plotted in (a). The arrow attached to the filled symbol is for charge 26, which should be outside the hornblende stability field. Dotted lines are the inferred positions for the stability curves of alkali feldspar, cummingtonite and biotite. It should be noted that the diagram is drawn for sulfur-free conditions. Addition of 0·2–0·3 wt % S would raise the thermal stability of both biotite and cummingtonite by ~10°C. The heavy vertical line represents the H_2O saturation curve. The solidus is taken from Ebadi & Johannes (1991) at 200 MPa.

diagram. Whatever the uncertainties of point locations (<0·4 wt % H_2O), the two projections can be considered as well constrained as far as pre-eruption conditions are concerned. Because the residual liquids are rhyolitic, an approximate location for the solidus of dacite in both diagrams is given by that of the haplogranite system at 200 MPa (Ebadi & Johannes, 1991).

Essential features of the phase relations are as follows. Plagioclase is the liquidus phase, crystallizing above 899°C for $aH_2O = 1$ (Fig. 2). The first appearance of quartz under H_2O-saturated conditions is around 750°C. Alkali feldspar is confirmed only in H_2O-poor runs, and its approximate boundary is drawn subparallel to the solidus curve. Hornblende is also stable above 899°C but it is restricted to the water-rich portion of the phase diagram. At 899°C, the abundance of hornblende is greatest at 6 wt % H_2O in melt (Table 2), which implies that its maximum thermal stability is not at H_2O saturation (Eggler, 1972; Holloway, 1973; Ghiorso, 1999). At 800°C, its place is taken by orthopyroxene when H_2O in melt falls to ~4·0 wt % (or XH_2O_{fluid} ~ 0·55) and, at 866°C, this change occurs at slightly higher water contents, around 5·0 wt % H_2O. At 899°C, orthopyroxene was not identified in run 43 (6·04 wt % H_2O in melt, Table 2), nor in any H_2O-saturated run at any temperature, or any run at 776–785°C. These observations imply a strong back bending of the orthopyroxene stability curve (Fig. 2). Although hornblende and orthopyroxene coexist in some runs, their relationship is basically that of a peritectic reaction. We do not have good constraints on their respective limits where they strike the solidus curve. Some sulfur-bearing charges (53 and 58, Table 2) crystallized orthopyroxene at 780°C under H_2O-rich conditions, which shows that addition of elemental sulfur produces a major expansion of its stability field. Given the scarce occurrence of clinopyroxene no attempt was made to draw its stability field, but it is certainly restricted to very dry conditions. Magnetite is the first Fe–Ti oxide to appear and its liquidus under water saturation probably occurs around 905°C. Ilmenite has a liquidus curve roughly parallel to that of quartz and crystallizes no higher than ~800°C at $aH_2O = 1$. Neither biotite nor ferromagnesian amphibole were produced in sulfur-free experiments performed with the dacite glass. In sulfur-bearing ones, Al-anthophyllite or gedrite, but not cummingtonite, crystallized at 780°C. This temperature is probably too high for cummingtonite in the dacite (Geschwind & Rutherford, 1992; Evans & Ghiorso, 1995). Only in sulfur-bearing runs does ferromagnesian amphibole (orthorhombic) give way to orthopyroxene with increasing temperature. Biotite appears only under sulfur-bearing and H_2O-rich conditions at 780°C. It was not found in sulfur- and CO_2-bearing runs (charge 53). Therefore, both the ferromagnesian amphibole and biotite occupy a restricted field in the low-temperature and high-water-content part of the diagram (Fig. 2). The presence of biotite at 747°C in the synthetic rhyolitic glass suggests that in the absence of sulfur it crystallizes at ~750°C (Table 2). In the dacitic bulk composition at ~780°C, anhydrite crystallized in charges at $fO_2 \geq$ NNO + 1·7, whereas pyrrhotite formed at NNO and NNO + 1. The sulfur-bearing runs on synthetic rhyolitic glass produced both anhydrite and pyrrhotite at 778°C at fO_2 = NNO + 1·4 and only pyrrhotite at 747°C at fO_2 = NNO + 1·3 (Table 2). Taken in combination, these results suggest a restricted co-stability field for anhydrite and pyrrhotite in the Pinatubo dacite magma, between NNO + 1·4 and NNO + 1·6 in the temperature range 780–750°C at 220 MPa. The presence of both anhydrite and pyrrhotite at 899°C and NNO + 1·2 (charge 42b) suggests that the co-stability field shifts toward lower fO_2 with increase in temperature. Finally, we note that the run at 778°C with the synthetic rhyolitic glass is almost at its liquidus for H_2O-saturated conditions, as only minute crystals of magnetite are present (Table 2).

Phase proportions

Mass-balance calculations show that plagioclase is the most abundant mineral (Table 2). At a given temperature, its abundance increases smoothly as the H_2O content of the melt decreases. Under water saturation, modal plagioclase is ~3 wt % at 899°C, rising to >30 wt % below 780°C. At melt H_2O contents >5 wt %, hornblende is second in abundance to plagioclase, except at 899°C under H_2O saturation. In contrast to plagioclase, modal hornblende is constant at 11–13 wt % over most of its stability field. Close to its stability limit, modal hornblende decreases swiftly, in concert with a complementary increase in orthopyroxene (Table 2). At 780°C, 220 MPa and aH_2O ~ 1, the addition of 1 wt % S to the system lowers modal hornblende by 4–5 wt % under all fO_2 conditions investigated (Table 2). Runs at 390 MPa show that the extra 170 MPa increases modal hornblende by 3–4 wt % (compare charges 65 and 8, Table 2), consistent with its expanded stability field at high pressure (e.g. Eggler, 1972), whereas modal plagioclase falls from ~30 to ~20 wt %. Orthopyroxene abundances are 10–11 wt %, similar to those of hornblende. At 220 MPa, biotite is <4 wt % whereas at 390 MPa it reaches nearly 8 wt % (Table 2). Modal magnetite averages 2 wt % and is never more than 3 wt %, whereas ilmenite seldom exceeds 1 wt %.

The fraction of melt declines smoothly with decreasing aH_2O at all temperatures (Table 2), allowing us to contour the phase diagram for wt % of melt fraction (Fig. 3a). The variation with temperature for H_2O-saturated conditions is non-linear (Fig. 3b). High temperature extrapolation places the liquidus about 910°C at $aH_2O = 1$ and 220 MPa, in agreement with Rutherford & Devine (1996). Below 780°C, H_2O-saturated, the melt fraction is calculated to be $\leq$55 wt %. At the same temperature, decreasing the melt H_2O content from 7 to 6 wt % reduces the melt fraction by ~10 wt % (Fig. 3a). Agreement with the natural Pinatubo white dacite is obtained at 770 $\pm$ 10°C for melt H_2O contents between 7 and 6 wt % (Fig. 3b).

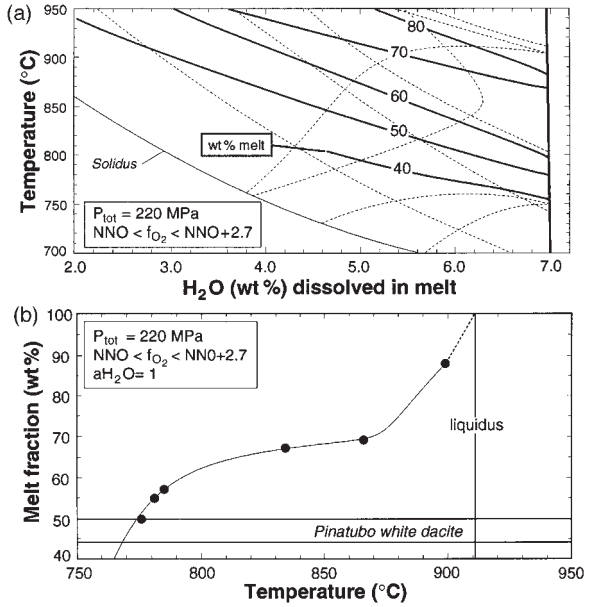

Fig. 3. (a) Variation of melt fraction (wt %) with temperature and melt H_2O contents. Dotted lines are the phase boundaries shown in Fig. 2a. (b) Variation of the melt fraction as a function of temperature under H_2O-saturated conditions at 220 MPa. The melt fraction of the crystal-rich Pinatubo dacite is from Luhr & Melson (1996). The liquidus is derived by extrapolation as shown.

Phase compositions

Plagioclase

Microprobe analysis of plagioclase in run products was difficult on account of its size (3–4 μm wide below 830°C and glass-cored at higher temperatures) and its poor contrast with residual glass in back-scattered electron (BSE) images. Consequently, contamination by matrix glass was not easily avoided. Compositions in Table 3 are single-spot or, where possible, average analyses, selected on the basis of a total close to 100% and Na + K + Ca > 1·9 per 16 oxygens. Many analyses with low totals and low alkalis displayed An/Ab ratios similar to the acceptable ones; although not included in Table 3, these analyses served to assess the compositional homogeneity of plagioclase in charges where more than one good analysis could not be obtained. In charges where multiple good analyses were possible, plagioclases in all but three runs displayed compositional variations of 1–3 mol % An, which is considered to be within analytical uncertainty given the problems mentioned above. In three charges (9, 20, and 51), compositional variation of plagioclase was greater, in two cases as much as 10% An. Not uncommonly, among several grains having compositions consistent with nearby runs in the T–aH_2O plane, there were a few albitic outliers, but not amounting to more than 10% of the total plagioclase population. Such compositions were typically restricted to coarse-grained individuals with no clear euhedral shape. Mass-balance calculations of modal plagioclase (Table 2) performed with the dominant plagioclase composition always yielded low residuals. A possible origin for this more albitic plagioclase is that it grew early in the run before the equilibrium water content of the residual liquid was attained, i.e. during hydration of the initially dry glass–liquid. Low water activities could have existed locally, enabling disequilibrium growth of albite-rich plagioclase, in keeping with their anhedral shape. The small amount of this plagioclase indicates that this

Table 3: Compositions of experimental plagioclases

Run:	8	9	16	17	18	19	20	21
n:[1]	6	4	3	2	3	5	3	1
SiO_2	58·05(16)[2]	59·44(1·5)	58·72(1·9)	57·66(24)	59·49(76)	58·28(35)	61·05(1·3)	60·04
Al_2O_3	25·40(45)	23·80(1·1)	23·83(94)	25·76(66)	24·24(41)	24·81(51)	23·66(1·0)	24·72
FeO	0·65(20)	0·72(29)	1·47(75)	0·44(18)	0·57(14)	0·73(25)	0·42(4)	0·32
CaO	8·00(22)	7·15(1·1)	7·94(36)	8·42(43)	7·61(41)	8·17(30)	6·83(1·1)	8·13
Na_2O	6·29(13)	6·66(68)	6·35(35)	6·01(10)	6·52(36)	6·17(16)	7·14(81)	6·48
K_2O	0·32(5)	0·42(7)	0·41(6)	0·36(4)	0·47(8)	0·41(6)	0·45(5)	0·32
Total	98·72	98·19	98·72	98·64	98·89	98·57	99·54	100·01
Ab	57·6(8)	61·2(5·6)	57·7(2·3)	55·2(1·1)	59·1(2·5)	56·3(1·2)	63·7(6·1)	57·9
An	40·5(9)	36·3(6·0)	39·8(2·4)	42·7(1·3)	38·1(2·3)	41·2(1·5)	33·7(6·0)	40·2
Or	1·9(3)	2·5(4)	2·5(3)	2·1(2)	2·8(5)	2·5(4)	2·7(2)	1·9
Run:	22	23	24	25	27	31	32	33
n:	5	5	5	1	1	2	2	2
SiO_2	56·54(82)	56·60(66)	58·33(69)	61·49	59·93	59·70(77)	60·90	56·72(26)
Al_2O_3	26·48(52)	26·22(63)	25·30(57)	21·71	23·59	23·46(31)	24·82	27·53(20)
FeO	0·43(8)	0·54(6)	0·53(12)	0·85	0·92	1·07(27)	0·78	0·41(10)
CaO	10·13(46)	10·00(37)	8·88(50)	7·06	7·70	7·36(44)	7·55	9·96(25)
Na_2O	5·41(27)	5·39(16)	5·97(26)	6·80	6·40	6·59(14)	6·71	5·58(17)
K_2O	0·23(8)	0·27(9)	0·36(7)	0·45	0·57	0·63(10)	0·48	0·24(1)
Total	99·22	99·02	99·36	98·37	99·11	98·80	101·24	100·81
Ab	48·5(2·2)	48·6(9)	53·7(2·5)	61·8	58·0	59·5(1·5)	59·9	49·7(1·4)
An	50·1(2·1)	49·8(1·1)	44·2(2·3)	35·5	38·6	36·7(2·1)	37·3	49·0(1·3)
Or	1·4(5)	1·6(5)	2·1(4)	2·7	3·4	3·8(6)	2·8	1·4(1)
Run:	34	35	36	42b	43	45	46	51
n:	2	1	1	3	3	3	3	2
SiO_2	58·12(30)	59·77	58·61	54·14(89)	57·74(94)	58·30(42)	59·91(89)	59·43(39)
Al_2O_3	26·77(12)	25·44	25·85	29·08(18)	25·67(87)	25·03(45)	24·61(58)	24·94(10)
FeO	0·74(12)	0·87	0·70	0·54(14)	0·78(29)	0·83(37)	0·55(10)	0·44(13)
CaO	9·67(35)	8·42	8·44	12·19(38)	9·11(68)	8·79(31)	8·00(39)	8·16(73)
Na_2O	5·63(12)	6·11	6·36	4·73(43)	5·71(10)	6·10(36)	6·35(11)	6·36(35)
K_2O	0·21(3)	0·39	0·30	0·14(2)	0·41(11)	0·41(7)	0·57(8)	0·44(5)
Total	101·14	100·99	100·26	100·83	99·42	99·46	99·99	99·76
Ab	50·6(1·3)	55·4	56·7	40·9(2·8)	51·8(1·9)	54·3(1·9)	57·0(1·3)	57·0(3·2)
An	48·1(1·5)	42·3	41·5	58·3(2·9)	45·7(2·6)	43·3(2·2)	39·7(1·6)	40·4(3·5)
Or	1·3(2)	2·3	1·8	0·8(1)	2·4(7)	2·4(4)	3·3(5)	2·6(3)
Run:	65	66	67	68	72	73		
n:	5	4	3	1	2	3		
SiO_2	58·38(10)	60·75(1·03)	59·38(41)	61·48	62·03(38)	62·13(82)		
Al_2O_3	25·56(71)	24·31(94)	24·25(93)	22·48	24·44(3)	23·97(62)		
FeO	0·85(51)	0·49(13)	0·67(27)	0·50	0·12(7)	0·06(6)		
CaO	8·21(40)	6·86(38)	7·52(52)	6·39	6·19(29)	6·09(48)		
Na_2O	6·46(22)	7·18(24)	6·64(6)	6·38	7·76(22)	7·55(38)		
K_2O	0·38(12)	0·45(14)	0·78(26)	1·27	0·53(9)	0·57(5)		
Total	99·84	100·04	99·24	98·50	101·07	100·37		
Ab	57·4(1·6)	63·8(1·2)	58·7(1·0)	59·4	67·3(0)	66·9(2·5)		
An	40·3(1·8)	33·6(1·7)	36·7(2·1)	32·9	29·7(6)	29·8(2·7)		
Or	2·2(7)	2·6(9)	4·6(1·5)	7·8	3·0(6)	3·3(2)		

[1]Number of analyses.
[2]Numbers in parentheses indicate one standard deviation of replicate analyses in terms of smallest units cited.

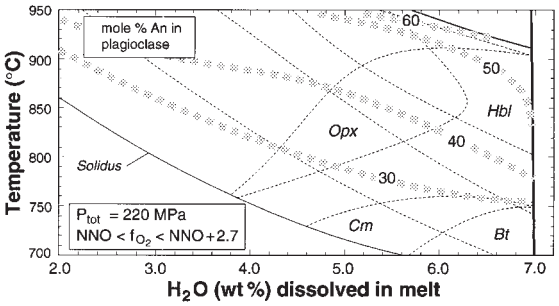

Fig. 4. Variation of the anorthite content of the plagioclase obtained in crystallization experiments (Table 3) with temperature and melt H_2O content. Dotted lines are the phase boundaries shown in Fig. 2a. Lines are fitted by hand.

experimental artifact should not significantly affect conclusions based on consideration of plagioclase compositions.

The anorthite content of plagioclase increases systematically with temperature and decreases with falling aH_2O, but no dependence on redox state was detected in the range of fO_2 investigated. Isopleths for An % drawn on the T–melt H_2O diagram are subparallel to the solidus and liquidus curves (Fig. 4). Under water-saturated conditions, plagioclase varies from ~60% An at 900°C close to the liquidus to ~37% at 760°C. Whereas a plagioclase with 40% An could crystallize at either 900°C with melt H_2O content ~3 wt % or at 780°C with 7 wt % H_2O in the melt, a plagioclase with 60% An requires both high temperature and melt water contents close to saturation (Fig. 4). The Or component of plagioclase increases with decreasing aH_2O and with decreasing temperature (Table 3), in other words correlates inversely with percent An, similarly reflecting distance from the solidus (or amount of sample crystallized). The series of runs at 899°C shows a threefold increase in Or content going from H_2O saturation down to a melt with 3 wt % H_2O (Table 3). Plagioclase crystallized at $aH_2O = 1$ at 390 MPa is similar in composition to that obtained at 220 MPa at the same temperature (Table 3; Or percent in samples 67 and 68 may partly reflect contamination by glass).

Amphibole

Amphibole crystallized in all sulfur-free runs is exclusively magnesiohornblende (Table 4). Analysis proved difficult only below 800°C. At higher temperatures, hornblende compositions were found to be homogeneous among several grains in each charge. At 759°C, and in several runs at ~780°C at 220 MPa, the hornblendes were so small that no single uncontaminated analysis was obtained. In these cases we removed the contribution from glass by assuming an original CaO content of 9–11 wt % in the hornblende, using the glass analysis obtained with a focused beam during the same analytical session. Apart from the 759°C runs, where apparently multiple sources of contamination rendered satisfactory analyses impossible, recalculated hornblendes gave good results as measured by restored anhydrous totals in the range 96–98%.

The composition of hornblende is sensitive to all the experimental variables investigated, including the amount of sulfur added. At fixed P–T–fO_2, a decrease in aH_2O produces a small but significant decrease in Al_2O_3, which reflects the increasing SiO_2 content of the coexisting melt. For example, at 899°C and 220 MPa, the Al_{tot} (p.f.u., 23 oxygens) decreases from 1·81 at H_2O saturation down to 1·64 for a melt H_2O content of 5·66 wt % (Fig. 5). Temperature variations also affect the Al_2O_3 content and, to a lesser extent, the *mg*-number [Mg/(Mg + Fe)]. From 780 to 899°C at 220 MPa and $aH_2O = 1$, Al_{tot} increases from 1·4–1·5 to 1·81 p.f.u., and the *mg*-number increases by 0·04 (Table 4). Higher temperature also increases the Na_2O content (from 1·6 wt % at 780°C to 2·2 at 899°C) and the TiO_2 content (from 1 to 2 wt %). The *mg*-number is primarily affected by changes in fO_2 and by the presence or absence of sulfur. In sulfur-free runs, an increase in fO_2 from NNO to NNO + 2·5 produces a increase in *mg*-number from 0·56 to 0·73 (Fig. 6). Introduction of sulfur into the system dramatically affects the *mg*-number of hornblende. In the field of sulfide crystallization, the *mg*-number is 0·1 larger for a given fO_2 in sulfur-bearing charges as compared with sulfur-free charges (Fig. 6). However, as sulphide gives way to anhydrite (fO_2 > NNO + 1·3), there is convergence of the *mg*-number of the hornblende (Fig. 6). Extrapolation of this trend beyond this fO_2 is not possible because adding sulfur under more oxidizing conditions destabilizes hornblende and gives rise instead to the ferromagnesian ortho-amphiboles anthophyllite and gedrite. Experiment 65 performed at 390 MPa, 780°C, and $aH_2O = 1$ may be compared with several runs at 220 MPa, ~780°C, and $aH_2O = 1$ to show that pressure increases the Al_2O_3 content from 8–9 to 10–11 wt %. This is comparable with the pressure effect obtained by Johnson & Rutherford (1989) for the Fish Canyon Tuff dacite. In other words, a pressure increase of ~200 MPa has an effect similar to that of a temperature increase of ~100°C.

Orthopyroxene

As for hornblende, the *mg*-number of orthopyroxene in run products reflects the fO_2 of the charge, temperature effects being minor (Fig. 7a, Table 5). For example, at NNO = + 0·56 (charge 37), the ferrosilite content of orthopyroxene is 40%. In a relatively oxidizing run (charge 24, NNO + 1·82), it is 29%. These compositions

Table 4: Compositions of experimental amphiboles

Run:	8	16[1]	17[1]	18[1]	19[1]	20	21	22	23	24	33
n:[2]	5	5	9	7	6	5	1	8	5	3	8
SiO_2	48·35(90)[3]	47·04(1·90)	48·97(1·14)	49·01(53)	49·45(1·94)	48·01(1·63)	52·57	46·68(1·41)	47·08(1·03)	48·77(1·92)	45·58(23)
Al_2O_3	9·10(30)	7·64(98)	7·12(86)	8·85(1·14)	7·56(85)	8·58(78)	6·89	9·95(34)	9·79(27)	8·91(73)	9·89(23)
FeO[4]	10·69(56)	17·63(1·82)	13·05(1·87)	13·88(76)	11·31(1·19)	12·45(49)	12·39	11·13(73)	10·44(47)	10·24(10)	13·48(36)
MgO	16·28(52)	12·77(1·47)	14·15(81)	12·06(83)	15·16(1·44)	13·85(89)	15·86	14·17(46)	14·52(76)	14·34(1·50)	14·23(26)
MnO	0·39(5)	0·31(12)	0·56(19)	0·31(12)	0·48(12)	0·38(16)	0·68	0·27(6)	0·30(10)	0·33(7)	0·29(6)
CaO	9·80(31)	9·00(—)	10·50(—)	9·00(—)	10·50(—)	9·61(31)	8·87	10·44(51)	10·46(41)	10·09(77)	10·40(9)
Na_2O	1·62(8)	1·65(54)	1·24(16)	1·64(35)	1·46(11)	1·38(15)	1·15	2·09(11)	2·07(6)	1·97(13)	1·99(13)
K_2O	0·33(8)	0·15(14)	0·23(10)	0·39(9)	0·22(14)	0·31(6)	0·21	0·40(10)	0·40(6)	0·44(17)	0·24(5)
TiO_2	1·08(6)	1·56(25)	1·49(29)	1·23(13)	1·57(23)	1·19(15)	1·47	1·67(18)	1·82(8)	1·77(21)	1·97(7)
Total	97·64	97·74	97·30	96·38	97·72	95·76	100·09	96·80	96·89	96·85	98·08
mg-no.[5]	0·73	0·56	0·66	0·61	0·70	0·66	0·69	0·69	0·71	0·71	0·65
Run:	34	35	42	42b	43	44	51	58	65	66	67
n:	3	1	6	6	6	1	7	1	9	5	7
SiO_2	46·48(18)	45·28	45·64(1·22)	47·67(1·25)	45·74(1·61)	45·12	49·38(1·36)	49·46	47·25(99)	49·07(1·03)	48·86(1·52)
Al_2O_3	9·25(28)	9·06	10·56(30)	10·15(1·11)	10·06(61)	9·55	8·37(1·10)	7·92	10·49(66)	9·57(56)	8·71(48)
FeO	14·11(24)	13·99	12·44(57)	8·17(62)	13·48(61)	14·21	11·43(51)	12·56	12·35(44)	12·13(75)	13·96(1·80)
MgO	13·79(31)	13·50	13·86(35)	17·32(96)	13·83(62)	14·16	14·58(39)	16·36	13·26(41)	13·87(95)	13·76(44)
MnO	0·36(4)	0·20	0·22(7)	0·30(10)	0·21(7)	0·22	0·43(12)	0·59	0·40(14)	0·41(8)	0·52(14)
CaO	10·19(12)	10·91	10·75(31)	10·27(61)	10·40(61)	10·92	9·83(55)	8·01	10·15(37)	9·65(50)	8·79(51)
Na_2O	2·12(9)	2·17	2·20(10)	2·08(16)	2·22(14)	2·16	1·64(25)	1·43	1·82(13)	1·66(10)	1·67(18)
K_2O	0·31(4)	0·38	0·37(7)	0·20(7)	0·33(10)	0·33	0·37(9)	0·23	0·40(8)	0·46(17)	0·31(7)
TiO_2	2·15(5)	2·03	1·96(17)	1·69(5)	2·26(26)	2·58	1·15(14)	1·22	1·02(10)	0·85(15)	1·06(25)
Total	98·77	97·52	97·99	97·86	98·52	99·26	97·18	97·18	97·14	97·67	97·63
mg-no.	0·63	0·63	0·66	0·79	0·65	0·64	0·69	0·70	0·66	0·67	0·64

[1]Recalculated hornblende.
[2]Number of analyses.
[3]Numbers in parentheses indicate one standard deviation of replicate analyses in terms of smallest units cited.
[4]Total Fe given as FeO.
[5]*mg*-number = Mg/(Mg + Fe).

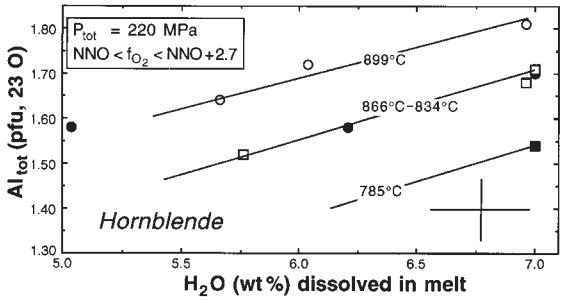

Fig. 5. Variations in total Al (p.f.u.) of hornblende obtained in crystallization experiments at 220 MPa with melt H_2O content and temperature. ■, 785°C; □, 834°C; ●, 866°C; ○, 899°C. The cross gives the average standard deviation.

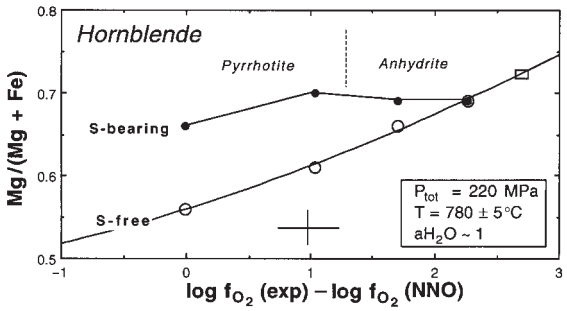

Fig. 6. Effect of fO_2 on the *mg*-number of experimental hornblende in S-free and S-bearing dacite at 780°C and 220 MPa. Also shown is the approximate boundary between pyrrhotite- and anhydrite-bearing charges. The curve for hornblende in the S-free system is a second-order polynomial fit: $\Delta NNO = -20{\cdot}206 + 51{\cdot}56(mg\text{-number}) - 27{\cdot}605(mg\text{-number})^2$ with a correlation coefficient $r^2 = 0{\cdot}995$. It has been used to estimate the fO_2 in the H_2O-saturated charges run at 785°C (open rectangle on the curve) and 834°C, listed in Table 2. The vertical bar is the average standard deviation; the horizontal bar is the maximum uncertainty on fO_2.

are broadly consistent with calculations of redox equilibrium between orthopyroxene and the Fe–Ti oxides (Evans & Ghiorso, 1995). Wo contents are mostly between 3 and 4%, and wt % Al_2O_3 <2. The higher Wo contents of orthopyroxene crystallized at 899°C (Table 5) are probably the result of contamination by either coexisting hornblende (charge 44) or undetected clinopyroxene (charge 45). More aluminous orthopyroxenes that crystallized in sulfur-bearing charges at 780°C follow the same trend as those crystallizing at higher temperatures in sulfur-free ones (Fig. 7a).

Biotite

Only in three runs performed with the dacite glass was biotite identified, all with added sulfur and at ~780°C, H_2O saturated. Analyses (Table 6) show SiO_2 contents in excess of 40 wt %, and are probably contaminated by glass. Structural formulae are deficient in alkalis (Na + K < 1·6 on a basis of 22 O) and possess significant amounts of octahedral Al. Recalculating the experimental compositions assuming 1·4 K p.f.u. (biotite in the Pinatubo rock displays K contents of 1·4–1·7 p.f.u.), gives structural formulae with little or no octahedral Al and an Na + K site occupancy between 1·7 and 2 p.f.u.

Biotite composition is primarily affected by fO_2, although its restricted occurrence makes it difficult to assess the effect of other intensive variables. At 780°C and 220 MPa, a decrease in fO_2 from NNO + 2·26 to NNO + 1·71 decreases the *mg*-number from 0·76 to 0·72 (Fig. 7b). Experiments carried out at approximately NNO + 2·5 suggest that a 170 MPa pressure increase may increase the Al_2O_3 content by ~2 wt % (Table 6).

Biotite was also obtained in a run performed with the synthetic rhyolitic glass at 750°C, 220 MPa, NNO + 1·3, and $XH_2O = 0{\cdot}9$, with no sulfur added (Table 2). Our analysis was highly glass contaminated, but adequate to show it is poorer in Mg (*mg*-number = 0·56) than biotite obtained with the dacite composition under similar P–T–fO_2–XH_2O conditions.

Fe–Ti oxides

Owing to their fine grain size and elongate habit, microprobe analyses of the rhombohedral phase (ilmenite and ferri-ilmenite) free from contamination by groundmass glass or other phases were difficult to obtain, except in runs above 800°C at aH_2O conditions distant from the solidus; the larger and more equant magnetite was easier to analyze. After calculating out glass contamination based on the SiO_2 value, and computing Fe^{3+} from formula constraints, the average total for all ilmenite or ferri-ilmenite analyses was 100·23%, and consistent results in terms of ilm/hem ratios were obtained by excluding all spot analyses with totals outside the range 97–103%. For magnetite, the average total was 98·56%, and so most analyses outside the range 97–101% were excluded. Average compositions of Fe–Ti oxides in our run products are listed in Table 7. In runs at high fO_2, standard deviations among spot analyses were 2% ilm and 1% usp, whereas at lower fO_2 they tended to be higher. In general, the scatter in compositions of Fe–Ti oxides reflects analytical and instrumental problems rather than any fundamental kinetic difficulty in growing the appropriate composition in crystallization runs.

For runs in the range 760–785°C the projected percent ilmenite in the rhombohedral phase coexisting with magnetite, normalized after Stormer (1983), shows a substantial decline between NNO + 1·0 and NNO + 1·7 (Fig. 8a). At NNO + 1·04, there is excellent agreement with redox conditions for coexisting oxides according to the formulations of both Andersen & Lindsley (1988) and Ghiorso & Sack (1991), whereas above NNO + 1·5 our measured compositions are substantially smaller in

Table 5: Compositions of experimental orthopyroxenes

Run:	24	25	26	27	34	35	36
n:[1]	2	3	1	2	8	8	3
SiO_2	53·99(148)[2]	53·66(80)	54·62	53·14(47)	53·59(41)	53·05(74)	52·91(9)
Al_2O_3	2·73(5)	1·74(32)	1·86	1·52(46)	1·71(33)	1·81(38)	1·51(36)
FeO[3]	17·56(105)	18·65(70)	20·49	20·55(105)	21·56(52)	22·63(51)	24·02(46)
MgO	23·49(40)	22·37(137)	20·62	22·41(50)	21·24(35)	20·21(106)	19·60(85)
MnO	0·76(7)	0·80(16)	0·79	0·65(21)	0·85(22)	0·67(13)	0·73(16)
CaO	1·72(22)	2·22(75)	1·32	1·54(29)	1·73(28)	1·64(16)	1·96(27)
Na_2O	0·21(1)	0·17(7)	0·24	0·10(8)	0·04(3)	0·09(12)	0·05(5)
TiO_2	0·23(1)	0·18(10)	0·20	0·20(13)	0·22(6)	0·19(8)	0·22(10)
Total	100·67	99·79	100·14	100·09	100·94	100·30	100·99
Wo	0·04	0·05	0·03	0·03	0·04	0·03	0·04
Fs	0·29	0·31	0·36	0·34	0·36	0·38	0·40
En	0·67	0·64	0·62	0·63	0·61	0·59	0·56

Run:	37	44	45	46	53	58
n:	5	2	2	1	5	5
SiO_2	52·93(96)	51·83(62)	53·73(22)	54·47	53·75(120)	52·82(94)
Al_2O_3	1·11(10)	2·17(43)	2·33(13)	2·16	3·51(99)	3·10(92)
FeO	24·52(49)	19·35(75)	21·71(14)	22·09	19·65(122)	17·84(174)
MgO	19·71(33)	21·32(57)	19·59(4)	17·31	21·89(166)	23·88(80)
MnO	0·51(9)	0·62(4)	0·63(9)	0·69	0·92(20)	0·99(11)
CaO	1·81(28)	3·59(54)	3·38(60)	4·36	0·73(16)	0·81(37)
Na_2O	0·02(1)	0·10(10)	0·18(1)	0·35	0·20(16)	0·16(33)
TiO_2	0·24(5)	0·26(1)	0·31(9)	0·35	0·13(5)	0·37(33)
Total	100·84	99·22	101·83	101·99	100·78	99·98
Wo	0·04	0·07	0·07	0·09	0·02	0·02
Fs	0·40	0·32	0·36	0·38	0·34	0·30
En	0·56	0·61	0·57	0·52	0·64	0·68

[1]Number of analyses.
[2]Numbers in parentheses indicate one standard deviation of replicate analyses in terms of least units cited.
[3]Total Fe given as FeO.

ilmenite content for a given fO_2 [for more details, see Evans & Scaillet (1997)]. Ilmenite in runs at NNO + 2·7 and NNO + 2·61 (charges 4 and 5) conducted with powdered natural dacite as starting material tended to retain its original composition except at the margins of grains where %ilm values approached and locally reached those (33% ilm for charge 4) produced in the crystallization runs under the same redox conditions (charges 8 and 9). This can be viewed as a half-bracket on the %ilm isopleth. Magnetite was not produced at $\log fO_2$ below NNO + 1·04. As in the case of ilmenite, the Ti content of magnetite at fO_2 above NNO + 1·04 (Fig. 8b) tends to smaller values than indicated by Andersen & Lindsley (1988) and Ghiorso & Sack (1991). Unlike ilmenite, the magnetite in charges 4 and 5 (natural dacite) largely re-equilibrated to the compositions produced in crystallization runs (6–7% usp)—in this case, a half-bracket on %usp. Contents of Al_2O_3 and MnO are comparable with those reported in the Fe–Ti oxide minerals of the natural dacite, whereas MgO is slightly larger (Table 7). The MgO content of ilmenite grown at low fO_2 is higher than in that grown at high fO_2, presumably a reflection of its TiO_2 content. Ilmenite in the Pinatubo dacite and in all our runs above NNO + 1·5 lies on the hematite side of the Fe–Ti order–disorder transition at 750–780°C, and the temperature is slightly above the top of the solvus in the pure system. We attribute the very large compositional shift in both Fe–Ti oxides over a small increment in ΔNNO to the rapidly changing thermodynamic properties of the geikielite-

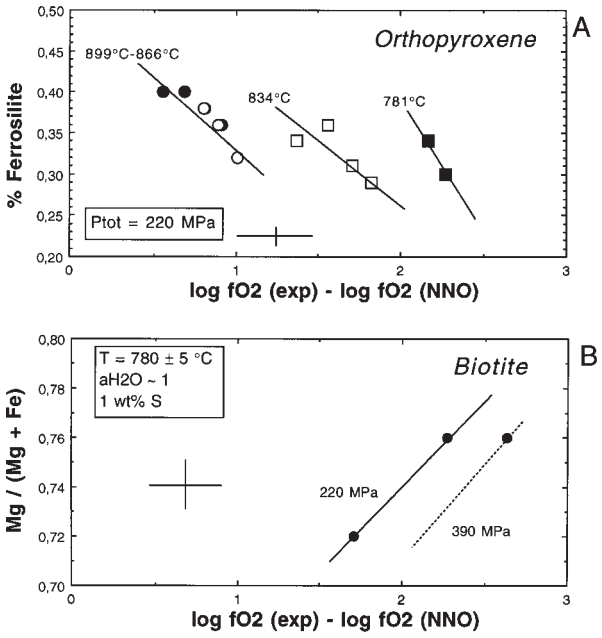

Fig. 7. (a) Variation of orthopyroxene composition with changes in fO_2 at several temperatures. ■, 781°C; □, 834°C; ●, 866°C; ○, 899°C. (Note that the 781°C trend corresponds to sulfur-bearing charges and that pyroxene is aluminous.) (b) Variation in biotite *mg*-number with fO_2 at the two investigated pressures and at 780°C. The vertical bar is the average standard deviation; the horizontal bar is the maximum uncertainty on fO_2.

Table 6: Compositions of experimental biotites

Run:	21	52	69
n:[1]	1	5	5
SiO_2	40·63	44·66(112)[2]	42·07(141)
Al_2O_3	14·29	14·73(34)	16·38(21)
FeO[3]	11·37	9·34(43)	9·60(46)
MgO	16·29	16·46(45)	16·80(70)
MnO	0·01	0·15(9)	0·09(13)
CaO	0·23	0·34(8)	0·18(13)
Na_2O	1·08	1·43(17)	1·64(10)
K_2O	6·97	6·55(19)	6·21(18)
TiO_2	2·51	2·31(12)	2·11(19)
Total	93·37	95·97	95·07
mg-no.[4]	0·72	0·76	0·76

[1]Number of analyses.
[2]Numbers in parentheses indicate one standard deviation of replicate analyses in terms of smallest units cited.
[3]Total Fe given as FeO.
[4]*mg*-number = Mg/(Mg + Fe).

bearing rhombohedral phase in the region close to the solvus (Evans & Scaillet, 1997).

Glass

Because of the high content of crystals, the residual glass could not be analyzed by microprobe in most experimental charges at low melt H_2O content. At 750°C, we could analyze the glass in the runs on synthetic rhyolite glass but not in those with the dacite bulk composition. In all cases, liquid compositions (Table 8) proved to be homogeneous within analytical uncertainty, displaying the smallest standard deviation of all analyzed phases. As expected, liquid composition is less evolved at higher T and aH_2O. Compositional changes with respect to T and melt H_2O content (Fig. 9) are due to the crystallization of the main crystalline phases (increase in SiO_2), plagioclase (decrease in CaO), and amphibole and Fe–Ti oxides (decrease in CaO, FeO, and MgO). Under water-saturated conditions at 780°C (Fig. 10), the melt has a slightly lower SiO_2 and higher Al_2O_3 content at 390 MPa (8·5 wt % H_2O) than at 220 MPa (7 wt % H_2O). At 780°C and 220 MPa, liquid compositions in melting experiments show good agreement with those obtained in crystallization runs, extending the trend displayed by the latter to low melt H_2O contents (Fig. 9). However, at higher temperatures differences can be seen between the compositions of melts produced in melting and crystallization experiments (see charges 33 and 41, Table 8). Variations of fO_2 in the range investigated here in sulfur-free runs do not seem to affect melt composition except for total FeO and MgO. In S-free charges the Fe/Mg ratio falls from 4·5 at NNO to two at NNO + 2·5, whereas in S-bearing charges the Fe/Mg ratio displays a constant value close to two. Finally, in S-bearing runs the CaO content of oxidizing runs is lower than that of reduced ones (0·5 wt % lower in CaO for a bulk S content of 1 wt %) because of anhydrite precipitation.

DISCUSSION

Comparison with previous work

Using a combination of melting and crystallization experiments, Rutherford & Devine (1996) presented a T–XH_2O phase diagram at 220 MPa for the Pinatubo white dacite. Our more extensive grid of experiments shows overall good agreement with their results for the major phases, plagioclase and hornblende, but, especially at high temperature and reduced aH_2O, we are able to define more precisely the phase relations of the dacite magma, and develop an understanding of the controls exerted on them by the variables fO_2 and aH_2O as well as T. For example, whereas the liquidi of the Fe–Ti oxides are not distinguished in the phase diagram of

Table 7: Compositions of experimental Fe–Ti oxides

Run:	8		9		16	17	18	
n:[1]	10	7	5	5	9	3	8	8
TiO_2	1·95(7)[2]	18·16(70	2·08(12)	19·21(20)	46·95(1·6)	50·70(37)	6·66(15)	44·35(1·9)
Al_2O_3	2·15(8)	0·69(12)	1·98(16)	0·54(19)	0·72(60)	0·29(27)	2·44(12)	0·36(21)
Fe_2O_3[3]	62·66(58)	63·98(2·1)	63·00(1·3)	61·35(1·7)	12·06(2·1)	6·96(2·9)	50·84(1·2)	16·20(2·9)
FeO[3]	29·12(47)	14·13(82)	29·84(30)	15·29(34)	38·03(1·8)	35·38(2·3)	33·67(66)	35·06(2·1)
MgO	2·00(8)	1·13(26)	1·80(33	1·01(7)	1·98(27)	4·83(1·3)	1·42(51)	2·30(30)
MnO	0·53(10)	0·19(4)	0·44(8)	0·19(14)	0·65(16)	1·58(37)	0·38(11)	0·70(13)
Total	98·41	98·28	99·15	97·58	100·39	99·75	95·40	98·98
% U/I[4]	5·44(21)	34·54(1·1)	5·82(33)	37·05(73)	88·07(2·1)	92·76(3·1)	20·57(1·1)	83·68(3·0)
Run:	19	20		21		22	23	24
n:	4	17	5	8	13	9	5	7
TiO_2	47·36(75)	3·91(14)	26·15(1·5)	3·92(24)	28·09(2·4)	3·88(10)	4·22(12)	4·66(20)
Al_2O_3	0·15(7)	2·05(63)	1·02(63)	2·50(38)	0·55(60)	2·63(12)	2·68(17)	2·30(15)
Fe_2O_3	10·94(79)	57·79(1·6)	51·34(1·8)	57·70(82)	45·82(4·2)	57·66(1·2)	57·71(43)	57·26(89)
FeO	34·62(91)	31·23(68)	20·93(1·3)	31·59(36)	22·56(1·7)	30·37(70)	30·51(29)	31·08(56)
MgO	3·71(10)	1·55(28)	1·36(28)	1·56(32)	1·42(22)	2·15(14)	2·40(10)	2·31(13)
MnO	1·34(12)	0·48(9)	0·16(17)	0·40(6)	0·16(13)	0·56(10)	0·65(6)	0·55(16)
Total	98·11	97·01	100·96	97·68	98·60	97·24	98·17	98·17
% U/I	88·64(66)	11·44(55)	48·98(1·8)	11·64(64)	53·65(4·1)	11·17(33)	11·88(40)	13·06(60)
Run:	24	25		26		27		31
n:	6	3	6	8	3	8	2	12
TiO_2	25·18(70)	4·82(20)	27·09(70)	5·07(18)	26·08(99)	5·74(20)	25·81(34)	4·07(18)
Al_2O_3	2·37(1·9)	1·23(38)	0·47(55)	0·92(58)	0·00	1·87(32)	0·33(10)	1·76(16)
Fe_2O_3	55·29(4·0)	58·27(1·7)	52·24(2·8)	58·41(1·8)	50·23(4·3)	55·73(2·2)	44·97(2·9)	58·28(1·1)
FeO	18·99(1·1)	31·86(8)	21·66(50)	32·48(69)	19·08(2·0)	32·63(1·1)	20·55(2)	32·09(50)
MgO	1·92(47)	2·00(43)	1·39(14)	1·81(49)	2·34(1·4)	2·06(69)	1·43(9)	1·28(34)
MnO	0·22(14)	0·34(14)	0·23(10)	0·34(17)	0·21(11)	0·41(10)	0·10(13)	0·40(9)
Total	103·98	98·51	103·07	99·02	97·64	98·43	93·19	97·89
%U/I	45·46(2·2)	13·22(63)	49·42(86)	13·8(83)	48·34(3·3)	16·14(1·0)	51·90(1·4)	11·87(59)
Run:	32	33	34	35		36	37	38
n:	11	6	5	1	5	6	1	1
TiO_2	4·18(19)	8·53(37)	10·75(13)	10·74	44·41(36)	46·43(84)	47·65	43·70
Al_2O_3	1·44(86)	3·21(19)	2·45(6)	2·45	0·41(19)	0·17(25)	0·37	0·12
Fe_2O_3	58·37(1·7)	48·72(78)	45·43(81)	45·94	17·40(44)	14·10(56)	7·93	10·64
FeO	32·39(61)	35·80(73)	37·99(25)	38·78	34·98(38)	36·91(66)	38·41	34·12
MgO	1·04(16)	1·86(10)	1·70(8)	1·52	2·45(8)	2·34(8)	2·34	2·60
MnO	0·56(12)	0·40(9)	0·49(6)	0·23	0·58(8)	0·66(20)	0·26	0·53
Total	97·97	98·53	98·80	99·65	100·22	100·61	96·96	91·70
%U/I	12·15(35)	25·90(67)	31·95(63)	32·00	82·68(30)	86·09(44)	91·91	88·44

Table 7: continued

Run:	41	42	44	45	46	51		52
n:	3	1	3	2	2	5	1	4
TiO_2	28·58(74)	6·45	10·71(33)	44·19(33)	44·89(86)	3·53(3)	23·06	3·51(3)
Al_2O_3	0·62(2)	3·70	2·58(8)	0·22(3)	0·33(12)	2·35(13)	0·57	3·13(8)
Fe_2O_3	46·93(1·9)	53·52	46·16(58)	19·84(1·2)	17·21(2·0)	60·62(85)	54·73	59·79(84)
FeO	23·12(51)	34·10	37·52(34)	34·03(7)	35·01(70)	31·52(58)	17·96	31·31(55)
MgO	1·34(8)	2·23	2·20(28)	2·98(15)	2·76(11)	1·79(13)	1·38	2·04(16)
MnO	0·19(5)	0·22	0·41(3)	0·39(10)	0·43(12)	0·56(1)	0·32	0·47(7)
Total	100·78	100·23	99·57	101·66	100·63	100·37	98·02	100·25
%U/I	53·58(1·5)	19·22	31·13(35)	80·46(96)	82·92(1·9)	9·93(1)	43·93	10·09(18)
Run:	52	53		58		65		66
n:	1	3	3	3	1	3	7	6
TiO_2	23·90	3·65(24)	25·11(30)	3·80(23)	25·81	1·85(11)	18·53(29)	2·07(8)
Al_2O_3	0·64	3·46(23)	0·62(5)	2·53(20)	0·63	2·32(7)	0·61(6)	2·38(10)
Fe_2O_3	54·28	59·08(1·2)	51·12(1·5)	58·76(60)	53·29	62·56(27)	64·21(1·8)	63·34(1·0)
FeO	18·66	32·14(22)	20·17(43)	31·53(44)	20·60	30·10(42)	15·11(33)	30·93(55)
MgO	1·42	1·70(4)	1·25(7)	1·77(8)	1·36	1·33(10)	0·77(4)	1·37(13)
MnO	0·31	0·42(8)	0·17(20)	0·37(5)	0·18	0·63(2)	0·18(10)	0·52(3)
Total	99·20	100·45	98·46	98·77	101·88	98·79	99·41	100·62
%U/I	45·05	10·86(76)	48·13(95)	11·04(80)	47·69(5·4)	5·37(36)	35·44(86)	5·94(17)
Run:	66	67		68	69		72	74
n:	1	4	4	7	2	3	3	1
TiO_2	19·37	2·45(7)	20·70(45)	2·53(15)	2·32(1)	21·11(20)	4·03(12)	2·89
Al_2O_3	0·73	2·20(9)	0·56(5)	1·86(7)	5·37(23)	1·04(1)	3·50(2)	2·74
Fe_2O_3	65·03	62·62(1·2)	60·29(1·0)	62·79(1·0)	60·37(29)	58·16(2·3)	57·00(19)	58·36
FeO	15·73	31·29(25)	17·05(28)	30·98(45)	31·02(17)	16·82(41)	33·86(24)	32·24
MgO	0·87	1·35(10)	0·78(4)	1·37(24)	2·06(10)	1·14(8)	0·84(1)	0·61
MnO	0·14	0·43(43)	0·18(12)	0·69(10)	0·43(1)	0·13(12)	0·01(2)	0·05
Total	101·87	100·36	99·56	100·22	101·58	98·41	99·24	96·90
%U/I	36·13	7·04(26)	39·63(56)	7·11(40)	7·18(7)	40·57(1·2)	12·91(34)	8·44

[1]Number of analyses.
[2]Numbers in parentheses indicate one standard deviation of replicate analyses in terms of smallest units cited.
[3]Fe^{3+} and Fe^{2+} calculated from formula constraints.
[4]U, mol % of ulvöspinel in the spinel oxide; I, mol % of ilmenite in the rhombohedral oxide. Both calculated using the normalization procedure of Stormer (1983).

Rutherford & Devine (1996), our data show that ilmenite first appears 50°C or more below magnetite, the latter belonging to the liquidus phase assemblage under water-saturated conditions. Hornblende appears on the liquidus at slightly over 900°C, as in the study by Rutherford & Devine (1996), but its modal variations suggest a temperature maximum at aH_2O ~0·9 rather than 1·0, and an absence of hornblende at melt H_2O contents lower than 4–5 wt %.

Our results on S-free dacite show that orthopyroxene and hornblende, except at high aH_2O, are related to each other by a peritectic reaction. At values of fO_2 sufficiently high to stabilize anhydrite, we find that the addition of small amounts of S has a noticeable effect on the occurrence of orthopyroxene, ferromagnesian amphibole, and biotite. For example, the addition of 0·32 wt % S (charge 58) is sufficient to extend the field of orthopyroxene down to 780°C at $aH_2O = 1·0$,

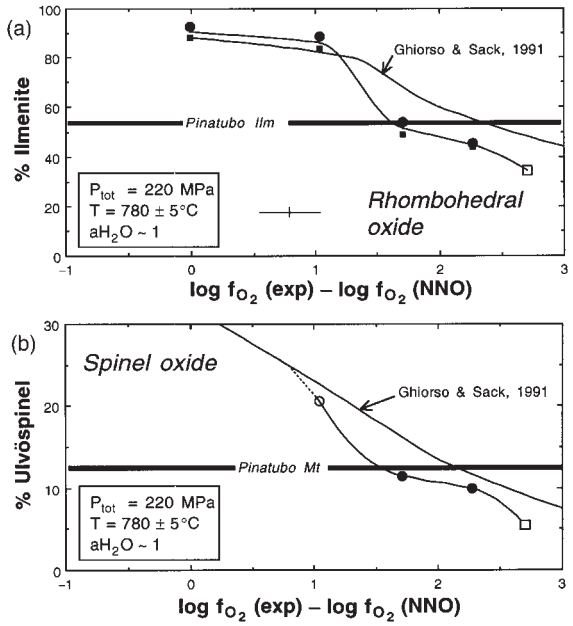

Fig. 8. (a) Variation of the ilmenite content of experimental rhombohedral oxide with fO_2 for H_2O-saturated runs at 780 ± 5°C. It should be noted that at NNO (S-free and S-bearing) and at NNO + 1 (S-bearing) there is no coexisting Fe–Ti spinel. (b) Variation of the ulvöspinel content of experimental Fe–Ti spinel with fO_2 for H_2O-saturated runs at 780 ± 5°C. ○, S-free runs; ●, S-bearing runs. □, the charge whose fO_2 has been estimated using the hornblende composition and the empirical relation of Fig. 6; ■, S-free runs. The thick bold lines represent the average compositions of Pinatubo oxides (Imai *et al.*, 1993; Hattori, 1996; Pallister *et al.*, 1996; Rutherford & Devine, 1996). The vertical bar is the average standard deviation of experimental oxide analyses; the horizontal bar is the maximum uncertainty on fO_2.

basically in agreement with Rutherford & Devine (1996). In runs at 780°C with more added S, we find orthorhombic ferromagnesian amphibole (Al-anthophyllite and gedrite), but not cummingtonite. These results make sense because simple mass-balance calculations show that 1 wt % S, for example, is capable of forming 4·2% anhydrite, taking at the same time all the CaO (~1·5 wt %) needed to form the typical 15% modal amounts of hornblende. A comparable sensitivity to S content also affects the presence of biotite. Rutherford & Devine (1996) reported a biotite liquidus temperature of ~ 850°C for $aH_2O = 1$, whereas in S-free runs we produced biotite only in rhyolite liquid at 747°C (charge 72). With added S, however, we find biotite in dacite at 780°C, and cannot rule out stable biotite at higher temperatures (e.g. 800–860°C).

Whereas cummingtonite was not detected in any of our sulfur-free experiments, Rutherford & Devine (1996) were able to define a small stability field for this phase (although no composition was provided), with a maximum thermal stability of ~790°C at 220 MPa. Both relict and newly grown cummingtonite were identified optically (M. Rutherford, personal communication, 1996). In our study, experiments performed with addition of sulfur at 780°C, $aH_2O = 1$ and NNO + 1·7 to NNO + 2·3 show that Al-anthophyllite or gedrite crystallizes in place of calcic amphibole as soon as the amount of S in the system exceeds 0·3–0·4 wt % (compare charges 52 and 58). These observations show that there is no kinetic problem in experimentally crystallizing ferromagnesian amphibole, but that its occurrence (whether cummingtonite, Al-anthophyllite, or gedrite) is critically dependent on the normative ratio Mg/Ca silicate in anhydrite-producing runs at high fO_2. Thus, in S-free Pinatubo dacite, there is no reaction relation between orthopyroxene and ferromagnesian amphibole, and in fact no evidence for the presence of the latter mineral at all. We conclude that the appearance of cummingtonite (*mg*-number = 0·71) in the Pinatubo dacite magma demands very specific conditions, namely $fO_2 <$ NNO + 2, high aH_2O (but not necessarily equal to 1·0), S present but not more than ~0·4 wt % and $T \leq 780$°C. Rutherford & Devine (1996) observed cummingtonite in their experiments because they used unfused natural rock as starting material, which, in contrast to our dry-glass starting material, contained enough sulfur to stabilize cummingtonite.

The most serious discrepancy between the two phase diagrams concerns the quartz boundary. The quartz liquidus temperature at $aH_2O = 1$ is ~70°C higher and the dT/daH_2O slope much flatter in the Rutherford & Devine (1996) phase diagram than in ours. A correct assessment of the quartz stability field is important because, although present in very low modal amounts, quartz is ubiquitous in the products of the climactic eruption (Bernard *et al.*, 1991, 1996; Fournelle *et al.*, 1996; Hattori, 1996; Luhr & Melson, 1996; Pallister *et al.*, 1996; Rutherford & Devine, 1996), and is one of the most important containers of glass inclusions used to assess pre-eruption conditions (Westrich & Gerlach, 1992; Wallace & Gerlach, 1994; Gerlach *et al.*, 1996; Rutherford & Devine, 1996). Although in our experiments the first appearance of quartz is readily detected, bracketing reversals were not performed. Therefore, two alternative explanations for the discrepancy are possible: sluggish nucleation of quartz (in the crystallization experiments) or low quartz dissolution rates (in the melting experiments). We believe that the first possibility is unlikely, however, because reversed crystallization experiments performed in more silicic systems under similar P and T conditions using the same procedure as here have clearly shown that the use of dry glass as starting material enhances the nucleation of tectosilicates (e.g. Pichavant, 1987; Holtz *et al.*, 1992). In these more silicic systems, phase boundaries located using forward experiments are within 15°C of those constrained by reversal experiments. In contrast, quartz is known to be one of the slowest

Table 8: Compositions of experimental glasses (normalized to 100 wt % anhydrous)

Run:	4	5	6	8	9	16	17	18
n:[1]	7	6	6	7	4	6	9	6
SiO_2	75·96(54)[2]	76·61(41)	78·38(38)	75·54(40)	77·83(59)	75·46(31)	75·93(99)	75·61(97)
Al_2O_3	14·05(10)	13·57(24)	12·50(13)	14·38(13)	13·18(8)	13·96(27)	14·04(28)	14·20(37)
FeO[3]	0·90(4)	1·00(10)	0·69(15)	1·04(15)	0·98(11)	1·01(14)	0·87(37)	1·15(14)
MgO	0·41(5)	0·36(4)	0·16(3)	0·38(13)	0·32(8)	0·70(24)	0·54(26)	0·40(27)
MnO	0·09(5)	0·06(5)	0·06(7)	0·07(6)	0·03(6)	0·12(6)	0·08(7)	0·06(5)
CaO	1·78(5)	1·47(10)	0·93(11)	1·95(18)	1·40(23)	2·09(26)	2·00(30)	1·94(13)
Na_2O	3·97(13)	3·83(10)	3·55(11)	3·69(42)	3·09(34)	3·64(16)	3·60(17)	3·49(35)
K_2O	2·71(6)	2·93(12)	3·62(16)	2·78(18)	3·07(6)	2·76(13)	2·73(10)	2·94(12)
TiO_2	0·15(4)	0·17(6)	0·12(6)	0·17(5)	0·10(6)	0·26(8)	0·23(9)	0·22(5)
H_2O[4]	7·43	6·48	6·56	7·88	7·57	7·42	7·76	7·94
Total[5]	90·40	91·79	91·68	89·64	90·17	90·40	89·85	89·55
Run:	19	20	21	22	23	24	25	33
n:	10	5	9	6	4	5	1	4
SiO_2	76·16(62)	75·69(75)	77·08(23)	73·59(54)	74·46(28)	75·09(90)	75·94	73·25(23)
Al_2O_3	14·27(37)	14·04(34)	14·04(16)	15·61(13)	15·28(14)	14·07(17)	12·85	15·72(62)
FeO	0·95(32)	1·27(33)	0·95(18)	1·60(16)	1·01(22)	1·68(7)	1·26	1·81(13)
MgO	0·39(33)	0·39(18)	0·34(7)	0·41(10)	0·27(8)	0·31(4)	0·54	0·27(11)
MnO	0·05(5)	0·10(6)	0·09(6)	0·06(5)	0·09(9)	0·08(6)	0·16	0·06(4)
CaO	1·74(15)	1·92(13)	1·53(10)	2·15(13)	1·93(18)	1·78(13)	2·03	2·26(5)
Na_2O	3·36(20)	3·53(19)	3·41(13)	3·84(18)	4·10(8)	3·80(50)	3·82	3·88(15)
K_2O	2·87(20)	2·80(11)	2·40(9)	2·41(8)	2·52(7)	2·86(6)	3·17	2·49(5)
TiO_2	0·23(8)	0·26(14)	0·16(5)	0·33(8)	0·35(2)	0·32(8)	0·22	0·26(3)
H_2O	8·11	8·22	8·09	7·80	7·76	6·56	6·99	7·78
Total	89·24	89·03	89·28	89·79	89·85	91·69	91·07	89·04
Run:	34	35	36	41	42	42b	43	44
n:	7	4	4	8	8	7	10	9
SiO_2	74·15(67)	74·17(82)	74·29(76)	71·16(41)	68·05(60)	68·84(64)	69·65(99)	70·77(88)
Al_2O_3	14·67(23)	14·30(23)	13·98(17)	15·92(20)	16·69(23)	16·85(13)	15·92(23)	15·25(30)
FeO	1·95(43)	1·86(19)	1·98(10)	2·48(18)	3·34(22)	2·26(22)	3·15(21)	2·91(20)
MgO	0·28(9)	0·26(10)	0·29(7)	0·70(7)	1·08(8)	1·18(5)	0·90(4)	0·76(11)
MnO	0·10(6)	0·09(6)	0·06(7)	0·08(8)	0·08(8)	0·10(6)	0·08(7)	0·03(5)
CaO	2·03(11)	1·92(4)	2·08(41)	2·90(11)	3·96(13)	4·03(10)	3·34(11)	2·95(21)
Na_2O	3·78(13)	4·03(18)	3·84(11)	4·20(15)	4·61(23)	4·58(24)	4·59(11)	4·52(16)
K_2O	2·66(8)	3·07(9)	3·15(13)	2·23(8)	1·82(10)	1·82(11)	1·99(9)	2·33(8)
TiO_2	0·38(7)	0·31(5)	0·32(8)	0·32(8)	0·37(7)	0·33(4)	0·38(8)	0·47(7)
H_2O	6·99	5·82	6·85	7·97	6·96	6·24	6·04	5·66
Total	90·43	92·15	90·64	88·69	90·47	91·56	91·85	92·36

dissolving minerals in silicate melts. In some experiments Rutherford & Devine (1996) used a starting material previously annealed at 860°C, but this annealing was performed at 100–130 MPa, presumably in the quartz stability field or close to it. The high-temperature position of the quartz liquidus curve in the Rutherford & Devine (1996) phase diagram may thus result from the persistence of quartz outside its stability field owing to its slow melting kinetics, especially at temperatures below 800°C. For these reasons we believe that our quartz liquidus curve more accurately expresses the equilibrium position than that of Rutherford & Devine (1996).

Conrad *et al.* (1988) determined the phase relations of a natural dacite whose bulk composition is very similar

Table 8: continued

Run:	45	46	50	51	52	53	58	65
n:	4	4	6	7	5	4	4	7
SiO_2	72·90(34)	73·52(84)	69·93(29)	75·60(79)	75·43(62)	77·55(48)	76·56(1·45)	74·94(48)
Al_2O_3	14·38(47)	14·04(58)	16·06(15)	14·64(21)	14·79(11)	13·77(38)	13·52(34)	15·44(10)
FeO	2·47(14)	2·32(24)	2·33(17)	1·18(9)	1·13(36)	1·19(20)	1·20(12)	0·88(16)
MgO	0·57(10)	0·53(22)	1·07(6)	0·31(10)	0·53(26)	0·39(3)	0·34(11)	0·25(6)
MnO	0·07(6)	0·04(5)	0·03(5)	0·03(3)	0·05(4)	0·08(7)	0·03(4)	0·06(5)
CaO	2·28(9)	2·33(22)	3·40(12)	1·84(10)	1·60(12)	1·08(8)	1·63(3)	2·33(28)
Na_2O	4·33(14)	4·19(13)	4·77(20)	3·49(30)	3·63(8)	2·86(31)	3·76(15)	3·53(18)
K_2O	2·63(14)	2·66(11)	2·12(7)	2·69(12)	2·57(3)	2·91(19)	2·75(8)	2·47(8)
TiO_2	0·37(7)	0·38(6)	0·29(5)	0·23(4)	0·27(8)	0·16(5)	0·21(12)	0·09(6)
H_2O	3·78	3·09	6·98	7·66	7·69	7·19	6·52	8·50
Total	94·62	95·37	90·44	89·28	89·22	90·10	91·16	87·55
Run:	66	67	69	72	73	74	75	
n:	6	7	7	6	7	6	6	
SiO_2	76·18(28)	77·31(84)	74·61(48)	78·10(56)	78·10(70)	78·56(44)	79·18(87)	
Al_2O_3	14·46(4)	13·20(19)	16·38(18)	13·05(7)	13·10(20)	12·44(13)	12·62(17)	
FeO	0·96(15)	0·99(12)	0·98(11)	0·78(11)	0·09(7)	0·93(8)	0·28(13)	
MgO	0·31(7)	0·25(2)	0·59(5)	0·22(2)	0·29(2)	0·20(2)	0·20(2)	
MnO	0·02(3)	0·07(5)	0·07(6)	0·04(4)	0·02(3)	0·07(5)	0·04(5)	
CaO	1·74(5)	1·57(17)	1·97(17)	0·86(5)	0·70(9)	1·25(8)	1·09(10)	
Na_2O	3·28(14)	3·35(11)	3·75(18)	3·10(11)	3·40(7)	3·42(15)	3·47(19)	
K_2O	2·88(15)	3·10(20)	1·52(7)	3·78(16)	4·21(15)	3·03(13)	3·01(7)	
TiO_2	0·16(3)	0·15(5)	0·13(4)	0·07(8)	0·10(5)	0·11(4)	0·11(2)	
H_2O	8·08	7·27	8·15	6·38	6·35	7·01	6·90	
Total	88·47	89·96	88·32	91·35	91·38	90·40	90·57	

[1]Number of analyses.
[2]Numbers in parentheses indicate one standard deviation of replicate analyses in terms of smallest units cited.
[3]Total Fe given as FeO.
[4]H_2O determined by using the by-difference method before correction for quench effects. Corrected water contents are listed in Table 2 (see text).
[5]Original probe total, after correction for alkali loss.

to that of Pinatubo. Their experiments were performed at 1000 MPa and fO_2 close to that defined by the fayalite–magnetite–quartz solid buffer. They also used dry glasses as starting material. Comparison of their phase diagram with ours shows that hornblende and orthopyroxene display the same peritectic relationships as in the S-free Pinatubo dacite, orthopyroxene replacing hornblende at high temperature and low aH_2O. Clinopyroxene also assumes the same position as in our phase diagram, and the tectosilicates display the same crystallization order, plagioclase liquidus temperatures being depressed by more than 200°C at high aH_2O. Biotite has a more prominent stability field, presumably as a result of the higher pressure. Cummingtonite was not found, consistent with its diminished stability at pressures >300–400 MPa (Geschwind & Rutherford, 1992; Nicholls *et al.*, 1992; Evans & Ghiorso, 1995; Rutherford & Devine, 1996). Overall, the results of Conrad *et al.* (1988) show that, as pressure increases, hornblende becomes the major silicate mineral on the liquidus under H_2O-rich conditions and that, apart from the effect of H_2O on temperature of crystallization of tectosilicates, the pressure increase does not significantly affect the phase diagram topology.

Comparison of our data with phase diagrams for other natural dacite–latite magmas at around 200 MPa (Merzbacher & Eggler, 1984; Rutherford *et al.*, 1985; Rutherford & Devine, 1988; Johnson & Rutherford,

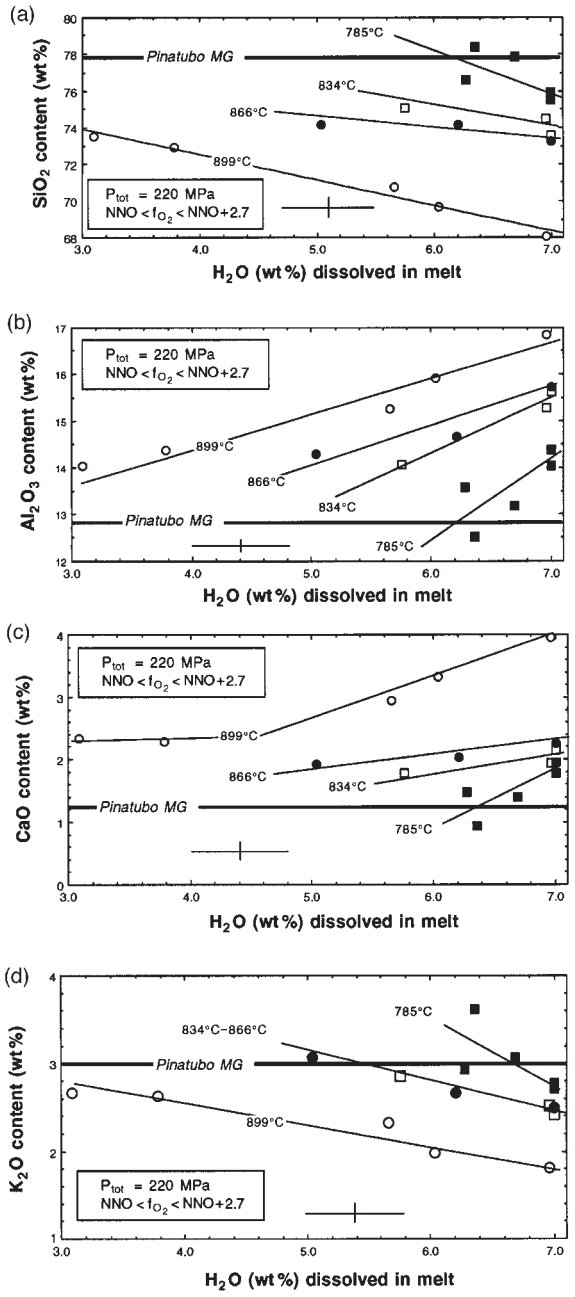

Fig. 9. Variations in melt composition (recalculated to 100 wt % anhydrous) with changes of temperature and melt H_2O content at 220 MPa. The bold horizontal lines show the oxide contents of the matrix glass of the Pinatubo crystal-rich dacite (Rutherford & Devine, 1996). It should be noted that at 785°C melt compositions obtained in melting experiments are also plotted (charges 4–6, Table 8). ■, 785°C; □, 834°C; ●, 866°C; ○, 899°C. The cross gives the average standard deviation of experimental glass analyses.

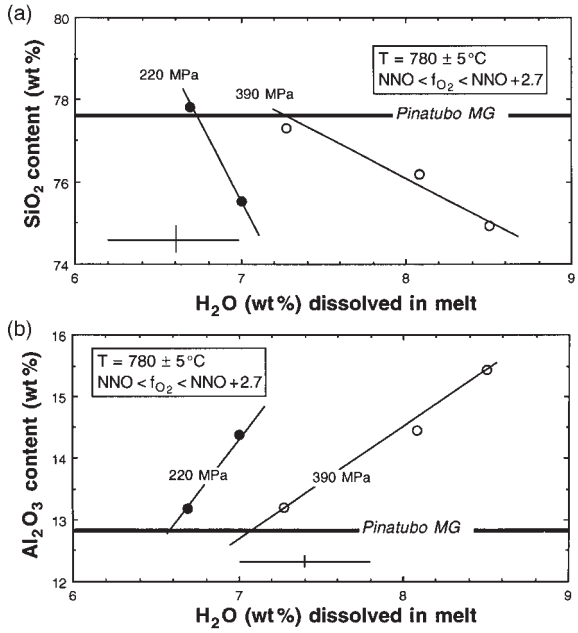

Fig. 10. Variations in melt composition (recalculated to 100 wt % anhydrous) with pressure and melt H_2O content at 780°C for (a) SiO_2 and (b) Al_2O_3. The bold horizontal lines show the oxide contents of the matrix glass of the Pinatubo crystal-rich dacite (Rutherford & Devine, 1996). The cross gives the average standard deviation of experimental glass analyses.

1989) shows that in all cases (Mount St Helens, Fish Canyon Tuff and Pinatubo) plagioclase saturation occurs between 880 and 910°C for $aH_2O = 1$. Variations in alkali element contents seem primarily to affect the position of hydrous mineral boundaries. For example, biotite in the Fish Canyon Tuff displays a very large stability field with a maximum thermal stability close to 900°C. Although both rocks have the same SiO_2 content, K_2O is more than twice as high in the Fish Canyon Tuff as in the Pinatubo dacite. Similarly, the Mount St Helens dacite has a slightly enhanced hornblende stability field compared with that of Pinatubo, owing to its Na_2O-rich character. A high Na_2O content has been shown to increase the stability of hornblende in basaltic compositions (Sisson & Grove, 1993).

Pre-eruption *P–T–f*O_2–*f*H_2O conditions

First-order constraints on pre-eruption conditions are provided by the natural phenocryst assemblage, assuming that it was at equilibrium (Rutherford & Devine, 1996) and the pre-eruption pressure was ~220 MPa (see below). Our phase diagram (Fig. 2) shows that the natural phase assemblage corresponds to a very restricted field of *T–X*H_2O conditions. The coexistence of plagioclase, hornblende, and Fe–Ti oxides requires temperatures lower than 830°C assuming $aH_2O = 1$ or 850°C assuming $aH_2O = 0{\cdot}5$. The lack of orthopyroxene phenocrysts restricts conditions to the water-rich portion of the phase

diagram, with melt H_2O content >5 wt %. Biotite crystallization requires conditions close to H_2O saturation. Although cummingtonite occurs predominantly as an overgrowth on hornblende phenocrysts, rare individuals in the matrix glass have been found (Fournelle *et al.*, 1996). In addition, cummingtonite contains glass inclusions similar in composition to those present in other phenocrysts, as shown by Rutherford & Devine (1996). Both facts suggest that cummingtonite and hornblende coexisted before eruption, which points to a pre-eruption temperature <800°C (Rutherford & Devine, 1996). The amount of quartz in the natural dacite is very small (<1%, Luhr & Melson, 1996; Pallister *et al.*, 1996) and its common rounded shape suggests some resorption before eruption (e.g. Pasteris *et al.*, 1996), possibly as a result of heating because of basalt underplating and injection (Pallister *et al.*, 1992). However, the close similarity between the compositions of glass inclusions and matrix glass in a given sample and from sample to sample (Westrich & Gerlach, 1992; Gerlach *et al.*, 1996; Rutherford & Devine, 1996) suggests that any remelting of the main body of the dacite magma was very limited. A significant remelting event would have destroyed the cummingtonite and forced the dacite magma back up its liquid line of descent, in which case the quenched residual melt would be less fractionated than the glass inclusions hosted by the quartz, a feature not observed in the crystal-rich dacite. For this reason, we believe that the Pinatubo dacite magma was minimally saturated with quartz just before eruption. The coexistence of quartz and hornblende implies temperatures no less than 850°C if water undersaturated, or less than 760°C at water saturation. Therefore, as shown by Rutherford & Devine (1996), from mineralogical considerations alone, it can be concluded that the Pinatubo dacite magma was at a maximum temperature of 780°C and that H_2O-rich conditions prevailed before eruption began. This conclusion is also indicated by the results obtained with the synthetic rhyolitic melt. This composition is very close to its liquidus at 778°C and H_2O-saturated conditions, which indicates that the pre-eruption temperature must have been lower that the experimental one, if $aH_2O \sim 1$. The fact that the low-temperature run performed with this synthetic composition lacks hornblende is interpreted to result from our synthetic composition being slightly Na_2O poorer than the natural residual glass [see matrix glass analyses of Rutherford & Devine (1996)].

Additional constraints on pre-eruption conditions are provided by a comparison of experimental and natural mineral compositions. Figure 11a plots Ti vs Na + K in hornblende, two components known to be sensitive to temperature. The natural hornblende compositions define a linear trend nearly parallel to the experimental one, and the vast majority of them correspond to an extrapolation of our experimental trend below 780°C. The main hornblende phenocryst population therefore has a composition consistent with a magma cooling over the range 780–740°C, or one at an average temperature of 760°C, conditions similar to those inferred from the phase assemblage constraints detailed above. The few hornblendes that indicate temperatures in the range 840–900°C are slightly outside our high-temperature experimental field, a shift that can be explained by a high-pressure fractionation event. To examine the role of pressure (Johnson & Rutherford, 1989; Schmidt, 1992), we plot Al_{tot} vs Na + K (Fig. 11b). Natural Pinatubo hornblende plots again in two distinct fields: the main population is characterized by Al_{tot} between 1 and 1·5 and Na + K <0·5, and the other group of analyses defines a high Al_{tot} and Na + K domain (see next section). Overall, the natural hornblendes define a trend that intersects the experimental one. Both temperature and pressure increase Al_{tot}. Our experimental data define the 220 MPa trend in the temperature range 780–900°C. Hornblende crystallizing at higher pressure would define a trend at higher Al_{tot}, as suggested by our 390 MPa experiments and other experimental studies (Johnson & Rutherford, 1989; Schmidt, 1992). Most of the natural population lies at the low-temperature end of the 220 MPa trend, showing that the crystallization pressure of this hornblende was no more than 220 MPa. The hornblende of this main group that falls below the experimental trend (Fig. 11b) can be explained by crystallization at both low pressure, roughly 180 MPa, and low temperature, 740–780°C. The hornblende compositions thus provide evidence of having resided in the cooler and shallower part of the erupted magma body, probably the upper semi-solidified shell of the dacite that was intruded by the basalt. The comparison of natural and experimental hornblende compositions therefore points to cooling and concomitant decompression of the dacite magma, down to conditions as low as 180 MPa and 740°C. Earlier conditions in the magma chamber are discussed later. The new refined and tightened pressure estimates are consistent with previous suggestions, based on seismic, petrological and experimental data, that the depth of the storage region before the 15 June eruption was about 6–10 km (Gerlach *et al.*, 1996; Mori *et al.*, 1996; Rutherford & Devine, 1996).

Rim compositions of plagioclase in the Pinatubo dacite range from An_{36} to An_{40}, but values as low as An_{27} have been reported. For conditions close to water saturation, this range also corresponds to temperatures between 780 and 740°C (Fig. 4a). There is no fundamental conflict between our experimental plagioclase compositions and those of the natural plagioclase. Both appear to have grown under conditions close to local equilibrium with the liquid. Thus, there seems no need to invoke a kinetic model of plagioclase rim growth for the Pinatubo dacite (Luhr & Melson, 1996).

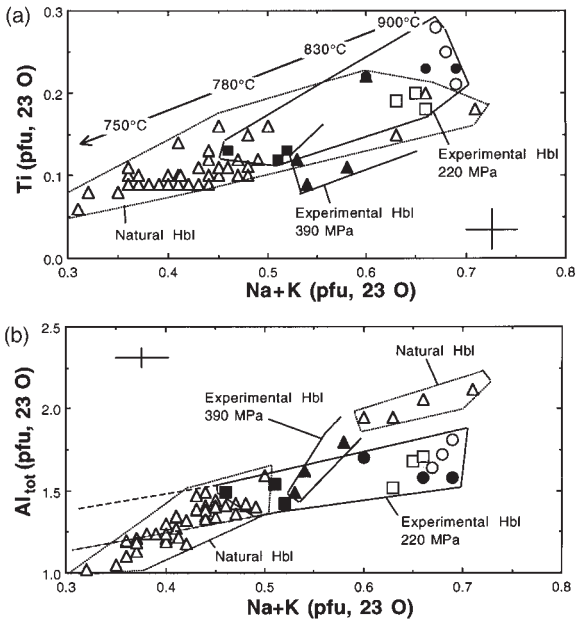

Fig. 11. Comparison of natural (△) and experimental (220 MPa: ■, 785°C; □, 834°C; ●, 866°C; ○, 899°C; 390 MPa: ▲) hornblende in terms of Ti vs Na + K (a) and Al_{tot} vs Na + K (b). For the experimental hornblende at 780°C, only non-corrected analyses were used, as the Na + K value is very sensitive to the recalculation procedure. It should be noted that the high-Al_2O_3 natural hornblende plots close to the hornblende crystallized at 780°C, 390 MPa and H_2O saturation. The higher Na + K of the natural hornblende can be attributed to their higher crystallization temperature. Natural hornblende analyses were obtained from our sample and from Bernard *et al.* (1996), Fournelle *et al.* (1996), Pallister *et al.* (1996) and Rutherford & Devine (1996). The cross gives the average standard deviation of experimental hornblende analyses.

Oxygen fugacity is best constrained by the experimental Fe–Ti oxide compositions. Most of our data under various fO_2 conditions were gathered at 780°C, whereas our estimated pre-eruption temperatures are slightly lower. This is a problem of marginal concern, however, as we are able to reproduce fairly closely the compositions of the natural coexisting ilmenite and magnetite in runs conducted at certain specific redox conditions (Evans & Scaillet, 1997, Fig. 3). Using our 780°C isotherm, the projected %ilm of ilmenite in the natural Pinatubo dacite (53–55%: Imai *et al.*, 1993; Hattori, 1996; Pallister *et al.*, 1996; Rutherford & Devine, 1996) corresponds to NNO + 1·5 to NNO + 1·7 according to Fig. 8a. Similarly, the usp content of magnetite in the natural Pinatubo dacite (12·5 ± 1·0%) corresponds to NNO + 1·5 to NNO + 1·7 (Fig. 8b). These estimates of fO_2 contrast with previous estimates of fO_2 based on the Fe–Ti oxides in Pinatubo white dacite pumice, which have fallen in the range NNO + 2·3 to NNO + 3·2 (Hattori, 1993, 1996; Imai *et al.*, 1993; Luhr & Melson, 1996; Pallister *et al.*, 1996; Rutherford & Devine, 1996). As these workers have recognized, these conditions are beyond the calibrated reach of the barometer. Corresponding temperatures based on oxide thermometry (before any empirical corrections) have been in the range 810–890°C. Depending on the experimental fO_2 we can in fact recover temperatures as high as 1000°C from our 780°C run products, and correspondingly excessively high fO_2 values, by using the Fe–Ti oxide thermobarometer uncritically beyond calibrated range. Thus, we believe that all the temperature estimates based on the Fe–Ti oxides in the Pinatubo dacites have been excessive. Our revised estimate of fO_2 (NNO + 1·5 to NNO + 1·7) is in much better agreement with fO_2 inferred from the composition of the cummingtonite rims on hornblende: Fe/(Fe + Mg + Mn + Ca) = 0·29 (Evans & Ghiorso, 1995; figs 9 and 10).

The last variable of interest is the pre-eruption water content of the melt. Comparison between the composition of the natural residual liquid and the experimental liquid as a function of its H_2O content provides an opportunity to constrain this factor. Figure 9 shows that, if the pre-eruption temperature was ~780°C (and P = 220 MPa), major element trends (SiO_2, Al_2O_3, CaO, K_2O) constrain the melt H_2O content to be 6–6·7 wt %. Higher pressures (Fig. 10) would require higher melt H_2O contents for the same temperature. A temperature of 750°C at 220 MPa would imply aH_2O = 1·0, or slightly less than this if P = 180 MPa. These estimates can be compared with those obtained from the analysis of H_2O by ion microprobe and IR spectroscopy in trapped glass inclusions (Westrich & Gerlach, 1992; Wallace & Gerlach, 1994; Rutherford & Devine, 1996). Only inclusions in quartz, and some in plagioclase, give H_2O contents in the range 6–7 wt %, close to our estimates. Glass inclusions hosted in other phenocrysts have much lower H_2O contents (3–4 wt %; see Westrich & Gerlach, 1992). These lower values would be inconsistent with the stability of hornblende (Fig. 2a) and with the An and Or contents of the plagioclase (Fig. 4). Furthermore, the variable H_2O contents of glass inclusions in the different phenocrysts of the Pinatubo dacite do not correspond to melts sampled along the liquid line of descent followed by the magma because their anhydrous compositions are remarkably similar to each other (Westrich & Gerlach, 1992; Rutherford & Devine, 1996). Instead, they merely reflect the greater or lesser efficiency of the different host minerals to minimize syn- or post-eruption loss of H_2O; hornblende being the most leaky, followed by magnetite and plagioclase, a conclusion also reached by Gerlach *et al.* (1996).

Thus, our data confirm the high H_2O content of the melt, with values close to saturation, as already concluded by others (Westrich & Gerlach, 1992; Gerlach *et al.*, 1996; Rutherford & Devine, 1996). This has led to the suggestion that, before eruption, the magma was fluid

saturated (Gerlach *et al.*, 1996), a situation that helps to explain the excess S observed during the eruption. In support of this conclusion, Wallace & Gerlach (1994) reported IR spectroscopic measurements of CO_2 in glass inclusions in quartz phenocrysts. The analyzed CO_2 contents (278–416 ppm) and melt water contents (>6 wt %) are large enough to saturate the magma at 220 MPa with a fluid phase. In Fig. 12, superimposed on the main phase boundaries from Fig. 2a, are isopleths of melt CO_2 content obtained from thermodynamic calculations of the fluid phase speciation using the solubility model of Silver *et al.* (1990) for H_2O and the solubility model of Blank *et al.* (1993) for CO_2. Fugacities of fluid species were modeled in the C–O–H system using the MRK equation of state of Holloway (1977) as modified by Flowers (1979). The calculation was carried out by fixing fH_2 and fH_2O (thus also fO_2, at ~NNO + 1·7, and the melt H_2O content), taking into account H_2O, H_2, CH_4, CO, and CO_2 as main species. By the Phase Rule, fixing the fugacities of two fluid species, in addition to T and P, fixes the fugacities of all remaining species (i.e. the C–O–H system is invariant). Knowing fCO_2, melt CO_2 contents were calculated after Blank *et al.* (1993). This method of calculation insures thermodynamic consistency between the fugacities of fluid species. The results show that, at the pre-eruption magma conditions, especially the H_2O content, inferred in this and other studies (see above), the melt CO_2 content must have been lower than 100 ppm, as found by Rutherford & Devine (1996). At 760°C, the CO_2 contents measured by Wallace & Gerlach (1994) would imply a much lower melt fraction (<30 wt %; compare Figs 12 and 3a) than that preserved by the natural dacite (45–50 wt %). They would also imply a coexisting fluid phase with much more CO_2 ($X H_2O_{fluid}$ < 0·6) than found in study of the volcanic cloud ($X H_2O_{fluid}$ = 0·82–0·86; Gerlach *et al.*, 1996). Therefore, unless the model of Blank *et al.* (1993) does not apply to the Pinatubo conditions (i.e. non-ideal mixing in the melt of CO_2 and H_2O, effects of additional components such as S), we conclude that the CO_2 contents determined by Wallace & Gerlach (1994) do not represent the average magmatic value for this species. One possibility is that their sample comes from the deepest part of the tapped magma body. For instance, using the above method of calculation we find that, at 300 MPa and 780°C, a rhyolitic melt saturated with a fluid phase with an $X H_2O$ = 0·8 would contain 342 ppm of CO_2. An increase in pressure accompanied by an appropriate decrease in the $X H_2O$ can keep the phase proportions constant (compare charges 9 and 67, Table 2). This does not preclude the magma from being volatile saturated, however. The $X H_2O_{fluid}$ restored by Gerlach *et al.* (1996) ranges from 0·82 up to 0·86. At 780°C this range crosses the quartz-in boundary, which is in agreement with minor quartz in the dacite. At 785°C for $X H_2O_{fluid}$ = 0·86 the residual

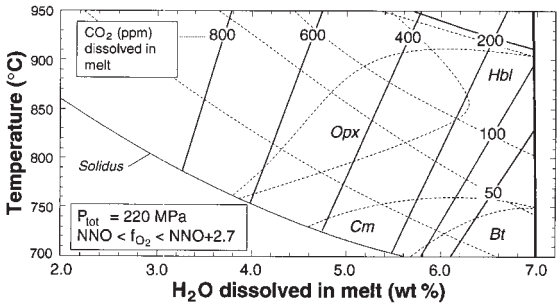

Fig. 12. Melt CO_2 contents calculated through homogeneous equilibria in the fluid phase in the C–O–H system with the modified Redlich–Kwong equation of state of Holloway (1977) and Flowers (1979) together with the solubility models of Silver *et al.* (1990) and Blank *et al.* (1993) for H_2O and CO_2, respectively. All calculations are for an fO_2 of NNO + 1·7. Also shown as dotted lines are the phase boundaries of Fig. 2a.

melt fraction is 47 wt %, as calculated for charge 9, or nearly identical to the natural one (~45–50 wt %; Luhr & Melson, 1996). In fact, charge 9 has almost all the attributes of the erupted magma with respect to the compositions of melt (including its water content), coexisting fluid phase, plagioclase, and hornblende, and major phase abundances, except that it lacks quartz (and cummingtonite, but this is due to the absence of S in the system). Either a lower temperature or a vapor phase poorer in H_2O would have allowed quartz crystallization (Fig. 2b). Considering the temperature range given by both plagioclase and hornblende compositions, the low Or content of the plagioclase, and the presence of biotite in the dacite (Fig. 2), the first possibility appears more likely. A temperature of ~760°C at an $X H_2O_{fluid}$ = 0·88 (~6·4 wt % H_2O in melt) would fulfill all the mineralogical, compositional and textural requirements inherent in the Pinatubo dacite. Slightly more H_2O-rich and slightly cooler conditions would also reproduce the natural phase assemblage.

Early magmatic history

Geochemical data show that the Pinatubo dacite has slab-melt characteristics, although other origins (e.g. fractionation of a more mafic parent magma such as a basalt) cannot at present be dismissed (Bernard *et al.*, 1996). Assuming that the magma was emplaced at ~220 MPa at a temperature higher than the pre-eruptive one, the principal mineral zonation (excluding that attributable to kinetic factors) should be explainable by variations in T, aH_2O, fO_2 and fS_2. We first consider plagioclase, as this mineral is primarily sensitive to changes in T and aH_2O. Hattori & Sato (1996) and Luhr & Melson (1996) have shown that plagioclase phenocrysts in the white dacite display complex patterns of compositional zoning,

including reversed zoning, abrupt changes in An content, and textural evidence of dissolution of earlier precipitated minerals. Despite these complexities, Hattori & Sato (1996) showed that the An and Or contents of the plagioclase display an inverse linear relationship [see also Bernard *et al.* (1996)], whose slope is clearly different from that of plagioclase found in the basaltic products ejected during the earlier stages of the eruption (Fig. 13). This plot shows that plagioclase composition, especially its Or content, is also controlled by bulk composition and it demonstrates unambiguously that the basalt ejected during the 1991 eruption cannot be the parent magma of the dacite magma, as already shown on geochemical grounds by Bernard *et al.* (1996) and Pallister *et al.* (1996). Our experimental plagioclase reproduces almost perfectly the natural trend, provided only H_2O-saturated conditions are considered (Fig. 13). At a given temperature, a decrease in aH_2O moves the plagioclase composition toward higher Or content (Fig. 13). Maxima in anorthite contents reported for plagioclase in the natural dacite seldom exceed An_{55} (Bernard *et al.*, 1996; Fournelle *et al.*, 1996; Luhr & Melson, 1996; Pallister *et al.*, 1996; Rutherford & Devine, 1996), which points to temperatures of ~900°C for $aH_2O = 1$ (Fig. 13). Therefore, whatever factors affected the plagioclase composition (crystal settling, magmatic convection, injection of fresh magma), Or and An in our experimental plagioclase suggest that the Pinatubo dacite magma continuously evolved under conditions close to H_2O saturation, with a maximum temperature close to the liquidus temperature at 220 MPa. Hattori & Sato (1996) also reported a few plagioclase compositions as calcic as An_{80}. Such calcic plagioclase is not reproduced under any set of reasonable T–XH_2O conditions explored in this study. As shown by Sisson & Grove (1993), calcic plagioclase requires a subtle combination of high-temperature and water-rich conditions. Extrapolation of our experimental trend of plagioclase compositions for $aH_2O = 1$ and 220 MPa would imply that the crystallization of An_{80} would require a temperature in excess of 950°C, which is higher than the liquidus in our experiments. An increase in pressure would further depress plagioclase liquidus temperatures, as shown by Conrad *et al.* (1988). For example, the plagioclase liquidus at 1000 MPa and $aH_2O = 1$ is 690°C and the plagioclase is An_{40}. Furthermore, the most calcic plagioclase produced in the latter study was An_{52}, for a maximum temperature of 950°C. Thus, the An_{80} plagioclase in the Pinatubo dacite is either a xenocryst or a phenocryst that crystallized in a more mafic bulk composition. In either case, the scarce occurrence of this calcic plagioclase suggests that it played a restricted role in the petrogenesis of the dacite magma, at least in the upper chamber where the magma was stored before eruption.

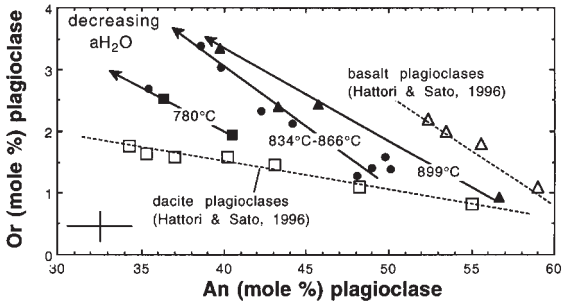

Fig. 13. Comparison of natural (open symbols) and experimental (filled symbols) plagioclase in terms of Or vs An. The natural plagioclase is taken from Hattori & Sato (1996) for both the dacite (□) and basalt (△). The arrows show the trends obtained by decreasing the melt H_2O content at the four main experimental temperatures investigated. ■, 780°C; ●, 834–866°C; ▲, 899°C. Only the plagioclase crystallized under H_2O-saturated conditions approaches the natural compositions. The slight departure from the dacite trend at 780°C probably results from glass contamination of the experimental plagioclase during microprobe analysis. The cross gives the average standard deviation of experimental plagioclase analyses.

Hornblende phenocrysts are generally more homogeneous than plagioclase but some phenocrysts with cores rich in Al_2O_3, Na_2O and TiO_2 have been found. Indeed, analyses carried out on a hornblende separate from our sample of white pumice show that they locally have Al_2O_3 contents in excess of 12 wt % (e.g. Bernard *et al.*, 1996; Fournelle *et al.*, 1996; Imai *et al.*, 1996). Two possible origins can be proposed for this hornblende: the first is that it is a remnant of an earlier mixing event between basalt and dacite. In support of this is the compositionally similar hornblende found in the 12 June dome andesite, thought to be a mixing product of basalt and dacite (Pallister *et al.*, 1996). The An_{80} plagioclase reported by Hattori & Sato (1996) could also correspond to such an event. The second possibility is that this high-Al_2O_3 hornblende records a higher-pressure stage of crystallization (Johnson & Rutherford, 1989; Schmidt, 1992). The hornblende that crystallized in our 390 MPa experiments indeed has a higher Al_2O_3 content than at 220 MPa, but only under H_2O-saturated conditions (run 65, Table 4). If the temperature effect on hornblende composition at 390 MPa is similar to that obtained at 220 MPa (Fig. 11b), then this hornblende implies conditions for this early crystallization stage at about 400 MPa, 840–900°C (Fig. 11b), and high aH_2O. The lack of intermediate compositions of hornblende suggests rapid transport of the magma between the two levels of crystallization. Additional experiments are clearly required, however, to see if this high Al_2O_3-hornblende can crystallize in the Pinatubo dacite at pressures higher than 200 MPa.

Although our revised estimate of fO_2 is lower by almost 1 log unit relative to previous estimates, the Pinatubo

dacite magma still falls at the high end of redox states displayed by silicic and intermediate arc magmas (Carmichael, 1991). Accordingly, the Pinatubo cummingtonite is more Mg-rich than cummingtonite in other siliceous volcanics (Evans & Ghiorso, 1995). The presence of sulfides has been taken as evidence for an earlier reduced stage in the magmatic evolution of the Pinatubo dacite (Hattori, 1993, 1996). However, our data show that, before eruption, the Pinatubo dacite had an oxidation state very close to, or perhaps slightly within, the co-stability field of anhydrite and pyrrhotite. Therefore, the dacite magma could well have been in equilibrium with both S-bearing minerals, although very close to the upper stability limit of pyrrhotite. At an fO_2 of NNO + 1·6, variations in fO_2 of <0·2 log unit may either stabilize or decompose any sulfide present in the magma. In addition, pyrrhotite in the dacite contains substantial amounts of Cu (Hattori, 1993, 1996), which could stabilize the sulfide to higher fO_2. The presence of sulfides in the dacite cannot thus be used as evidence for an earlier reduced stage. The S abundance of the Pinatubo magma has also been related to fluids discharging from underlying crystallizing basalts (e.g. Pallister *et al.*, 1996). According to Hattori (1993, 1996), such a process could explain the oxidized character of the Pinatubo dacite [see also Matthews *et al.* (1994)]. However, introduction of sulfur under any set of conditions relevant to the dacite petrogenesis increases the *mg*-number of Ca-amphibole except if fO_2 is above NNO + 2 (Fig. 6). Although no systematic study of hornblende compositional zonation has been made, a prominent Mg-rich overgrowth on Pinatubo hornblende is lacking. This suggests that, if S has an external origin, then it must have been supplied to the dacite magma under redox conditions similar to those prevailing before the eruption (~NNO + 1·7). In other words, an introduction of S is unlikely to have been responsible for the high oxidation state of the dacite magma. Finally, we note that plagioclase preserves evidence of conditions close to water saturation at all temperatures, a trend difficult to reconcile with an infiltration of the dacite magma by fluids emanating from underlying basalt. Long-term percolations of basaltic fluids will instead decrease the aH_2O in the overlying dacite, unless the crystallization of these basalts produces H_2O-rich fluids.

CONCLUDING STATEMENTS

This work shows that nearly all the major features of the crystal-rich variety of dacite erupted at Mt Pinatubo can be reproduced by phase-equilibrium experiments. The immediate implication is that equilibrium conditions most probably prevailed during the crystallization of the dacite magma in the upper storage chamber. If basalt injection triggered the eruption (Pallister *et al.*, 1996), then its thermal and chemical effects must have been minimal to preserve this equilibrium state. One way to account for this, as already suggested by Pallister *et al.* (1996), is to have a very short lag time between magma injection and eruption, which is in agreement with the proposed genetic link between the two phenomena (Pallister *et al.*, 1992). Phase proportions are reproduced as well, which shows that mechanical sorting did not occur upon eruption, a feature indicative of extremely fast cooling rates, sufficient to quench magmatic textures at the hand-specimen scale. As regards the early period recorded by the main minerals plagioclase and hornblende, both point to water-rich conditions during most of the crystallization period in the upper-crustal magma chamber. Plagioclase in particular indicates that the magma may have been near H_2O saturation very early in its history. This places constraints on the minimum amount of fluid phase that can be expected to coexist with the magma under pre-eruption conditions. If the magma had been H_2O saturated at 900°C, the melt would have contained nearly 7 wt % H_2O (Fig. 2a). At a pre-eruption temperature of 760°C, the magma is 40–50% crystallized, so the fluid phase coexisting with the magma may amount to ~3 wt %, which falls within the range calculated for other silicic eruptions (Wallace *et al.*, 1995). Obviously, this calculation neglects possible fluid loss by upward percolation driven by buoyancy. Its shows, however, that there is no need to call upon external fluids to explain some of the geochemical features of the dacite. Fluid migration and accumulation at the top of the magma chamber can be produced by the dacite magma on its own. In such a system, the deepest parts of the plumbing system may release and supply the excess volatiles to the upper reaches of the magma chamber. These fluids could scavenge the percolated magma of elements with elevated partition coefficients and concentrate them in apical portions of the system. Sulfur may have been one of them. The Pinatubo dacite thus provides one more example of the important role of H_2O in the petrogenesis of arc-magmas (e.g. Gaetani *et al.*, 1993). A related topic is the oxidized character of these water-rich magmas (e.g. Carmichael, 1991; Sisson & Grove, 1993). Although it is beyond the scope of this paper to discuss in detail the origin of the oxidized character, we note that there is no evidence to suggest that the redox state changed by several orders of magnitude during upper-crustal residence. On the other hand, excluding kinetic factors, the complex zoning pattern preserved by the plagioclase suggests that some sort of magma mixing occurred in the past history of the magmatic reservoir [see Hattori & Sato (1996)]. However, plagioclase displays a unique An vs Or trend (Fig. 13), which implies that during the entire period of crystal growth, the bulk composition of the host magma

did not change significantly. The control that bulk composition exerts on this compositional variable has been shown by Sato (1984). The only way to maintain the An vs Or relationship in a continuously replenished magma chamber is through injection of fresh magma with a bulk composition (including melt H_2O content) similar to the intruded one. The fact that basalt was injected into the cooling dacite pluton thus appears to have been probably fortuitous. As Pallister *et al.* (1996) have suggested, its main role was to overpressurize the volatile-rich cap of the crystallizing dacite pluton, which subsequently underwent explosion. If the dacite had been less crystallized, then probably mixing following basalt intrusion would have been much more effective. Within this context, the pre-eruption conditions of the volcanic event are pre-intrusion conditions as well. Finally, the Pinatubo event illustrates a situation where the eruption is not triggered by the continuous increase of pressure in the magma chamber through volatile exsolution as crystallization proceeds, as modeled by Tait *et al.* (1989) for silicic arc-volcanoes. In the latter model the pressure in the magma chamber increases upon volatile exsolution until the tensile stress of the host rock is exceeded. Although the Pinatubo volcano fulfills all the conditions to follow this pattern, it apparently did not occur.

ACKNOWLEDGEMENTS

We first of all would like to thank Dr R. S. Punongbayang and M. Martines, who provided the natural sample used for the experiments in this study, and Dr Bjorn Mysen, who provided the necessary information to contact the PHIVOLCS institute. B.W.E. thanks the CNRS and Région Centre for the support of a bursary during his stay in Orléans. Continuous discussions with M. Pichavant helped in understanding important features related to arc magmas. Thorough and helpful reviews were provided by James F. Luhr and Malcolm Rutherford. The editorial handling of Richard J. Arculus is gratefully acknowledged.

REFERENCES

Albarède, F. (1995). *Introduction to Geochemical Modeling*. Cambridge: Cambridge University Press, 543 pp.

Andersen, D. J. & Lindsley, D. H. (1988). Internally consistent solution models for Fe–Mg–Mn–Ti oxides: Fe–Ti oxides. *American Mineralogist* **73,** 714–726.

Arculus, R. J., Johnson, R. W., Chappell, B. W., McKee, C. O. & Sakai, H. (1983). Ophiolite-contaminated andesites, trachybasalts, and cognate inclusions of Mt. Lamington, Papua New Guinea anhydrite–amphibole-bearing lavas and the 1951 cumulodome. *Journal of Volcanology and Geothermal Research* **18,** 21–47.

Baker, L. & Rutherford, M. J. (1992). Anhydrite breakdown as a possible source of excess sulfur in the 1991 Mount Pinatubo eruption. *EOS Transactions, American Geophysical Union* **73,** 625.

Bernard, A., Demaiffe, D., Mattielli, N. & Punongbayan, R. S. (1991). Anhydrite-bearing pumices from Mount Pinatubo: further evidence for the existence of sulfur-rich silicic magmas. *Nature* **354,** 139–140.

Bernard, A., Knittel, U., Weber, B., Weis, D., Albrecht, A., Hattori, K. & Oles, D. (1996). Petrology and geochemistry of the 1991 eruption products of Mount Pinatubo (Luzon, Philippines). In: Newhall, C. G. & Punongbayan, R. S. (eds) *Fire and Mud. Eruptions and Lahars of Mount Pinatubo, Philippines*. Seattle: University of Washington Press, pp. 767–798.

Blank, J. G., Stolper, E. M. & Carroll, M. R. (1993). Solubilities of carbon dioxide and water in rhyolitic melts. *Earth and Planetary Science Letters* **119,** 27–36.

Bluth, G. J. S., Doiron, S. D., Schnetzler, C. C., Krueger, A. J. & Walter, L. S. (1992). Global tracking of the SO_2 clouds from the June, 1991 Mount Pinatubo eruptions. *Geophysical Research Letters* **19,** 151–154.

Burnham, C. W., Holloway, J. R. & Davis, N. F. (1969). Thermodynamic properties of water to 1000°C and 10 000 bar. *Geological Society of America Special Paper* **132,** 1–96.

Carmichael, I. S. E. (1991). The redox states of basic and silicic magmas: a reflection of their source regions. *Contributions to Mineralogy and Petrology* **106,** 36–64.

Carroll, M. C. & Rutherford, M. J. (1987). The stability of igneous anhydrite: experimental results and implications for sulfur behavior in the 1982 El Chichòn trachyandesite and other evolved magmas. *Journal of Petrology* **28,** 781–801.

Carroll, M. C. & Rutherford, M. J. (1988). Sulfur speciation in hydrous experimental glasses of varying oxidation states: results from measured wavelength shifts of sulfur X-rays. *American Mineralogist* **73,** 845–849.

Chou, I. M. (1987). Oxygen buffer and hydrogen sensor technique at elevated pressures and temperatures. In: Barnes, H. L. & Ulmer, G. C. (eds) *Hydrothermal Experimental Techniques*. New York: John Wiley, pp. 61–99.

Conrad, W. K., Nicholls, I. A. & Wall, V. J. (1988). Water-saturated and -undersaturated melting of metaluminous and peraluminous crustal compositions at 10 kb: evidence for the origin of silicic magma in the Taupo volcanic zone, New Zealand, and other occurrences. *Journal of Petrology* **29,** 765–803.

Devine, J. D., Sigurdsson, H., Davis, A. N. & Self, S. (1984). Estimates of sulfur and chlorine yield to the atmosphere from volcanic eruptions and potential climatic effects. *Journal of Geophysical Research* **89,** 6309–6325.

Devine, J. D., Gardner, J. E., Brach, H. P., Layne, G. D. & Rutherford, M. J. (1995). Comparison of microanalytical methods for estimation of H_2O contents of silicic volcanic glasses. *American Mineralogist* **73,** 845–849.

Ebadi, A. & Johannes, W. (1991). Beginning of melting and composition of first melts in the system Qz–Ab–Or–H_2O–CO_2. *Contributions to Mineralogy and Petrology* **106,** 286–295.

Eggler, D. H. (1972). Amphibole stability in H_2O-undersaturated calc-alkaline melts. *Earth and Planetary Science Letters* **15,** 28–34.

Evans, B. W. & Ghiorso, M. S. (1995). Thermodynamics and petrology of cummingtonite. *American Mineralogist* **80,** 649–663.

Evans, B. W. & Scaillet, B. (1997). The redox state of Pinatubo dacite and the ilmenite–hematite solvus. *American Mineralogist* **82,** 625–629.

Flowers, G. C. (1979). Correction of Holloway's (1977) adaptation of the Modified Redlich–Kwong equation of state for calculation of the fugacities of molecular species in supercritical fluids of geologic interest. *Contributions to Mineralogy and Petrology* **69,** 315–318.

Fournelle, J., Carmody, R. & Daag, A. G. (1996). Mineralogy and geochemistry of Mount Pinatubo anhydrite- and sulfide-bearing pumices from the SO_2-rich eruption of June 1991. In: Newhall,

C. G. & Punongbayan, R. S. (eds) *Fire and Mud. Eruptions and Lahars of Mount Pinatubo, Philippines*. Seattle: University of Washington Press, pp. 845–864.

Gaetani, G. A., Grove, T. L. & Bryan, W. B. (1993). The influence of water on the petrogenesis of subduction related igneous rocks. *Nature* **365,** 332–334.

Gerlach, T. M., Westrich, H. R., Casadevall, T. J. & Finnegan, D. L. (1994). Vapor saturation and accumulation in magmas of the 1989–1990 eruption of Redoubt volcano, Alaska. *Journal of Volcanology and Geothermal Research* **62,** 317–337.

Gerlach, T. M., Westrich, H. R. & Symonds, R. B. (1996). Pre-eruption vapor in magma of the climactic Mount Pinatubo eruption: source of the giant stratospheric sulfur dioxide cloud. In: Newhall, C. G. & Punongbayan, R. S. (eds) *Fire and Mud. Eruptions and Lahars of Mount Pinatubo, Philippines*. Seattle: University of Washington Press, pp. 415–434.

Geschwind, C. H. G. & Rutherford, M. J. (1992). Cummingtonite and the evolution of the Mount St Helens magma system. *Geology* **20,** 1011–1014.

Ghiorso, M. S. (1999). On the stability relations of hydrous minerals in water-undersaturated magmas. *American Mineralogist* (submitted).

Ghiorso, M. S. & Sack, R. O. (1991). Fe–Ti oxide geothermometry: thermodynamic formulation and the estimation of intensive variables in silicic magmas. *Contributions to Mineralogy and Petrology* **108,** 485–510.

Hansen, J., Lacis, A., Ruedy, R. & Sato, M. (1992). Potential climate impact of Mount Pinatubo eruption. *Geophysical Research Letters* **19,** 215–218.

Hansen, J., Ruedy, R., Sato, M. & Reynolds, R. (1996). Global surface temperature in 1995: return to pre-Pinatubo level. *Geophysical Research Letters* **23,** 1665–1668.

Hattori, K. (1993). High sulfur magma, a product of fluid discharge from underlying mafic magma: evidence from Mount Pinatubo. *Geology* **21,** 1083–1086.

Hattori, K. (1996). Occurrence and origin of sulfide and sulfate in the 1991 Pinatubo eruption products. In: Newhall, C. G. & Punongbayan, R. S. (eds) *Fire and Mud. Eruptions and Lahars of Mount Pinatubo, Philippines*. Seattle: University of Washington Press, pp. 807–824.

Hattori, K. & Sato, H. (1996). Magma evolution recorded in plagioclase zoning in 1991 Pinatubo eruption products. *American Mineralogist* **81,** 982–994.

Holloway, J. R. (1973). The system pargasite–H_2O–CO_2: a model for melting of a hydrous mineral with a mixed volatile fluid—I. Experimental results to 8 kilobars. *Geochimica et Cosmochimica Acta* **37,** 651–666.

Holloway, J. R. (1977). Fugacity and activity of molecular species in supercritical fluids. In: Fraser, D. (ed.) *Thermodynamics in Geology*. Dordrecht: D. Reidel, pp. 161–181.

Holloway, J. R. (1987). Igneous fluids. In: Carmichael, I. S. E. & Eugster, H. P. (eds) *Thermodynamic Modelling of Geological Material. Mineralogical Society of America, Reviews in Mineralogy* **17,** 211–232.

Holtz, F., Pichavant, M., Barbey, P. & Johannes, W. (1992). Effects of H_2O on liquidus phase relations in the haplogranite system at 2 and 5 kbar. *American Mineralogist* **77,** 1223–1241.

Holtz, F., Behrens, H., Dingwell, D. & Johannes, W. (1995). H_2O solubility in haplogranitic melts: compositional, pressure, and temperature dependence. *American Mineralogist* **80,** 94–108.

Hurwitz, S. & Navon, O. (1994). Bubble nucleation in rhyolitic melts: experiments at high pressure, temperature, and water content. *Earth and Planetary Science Letters* **122,** 267–280.

Imai, A., Listanco, E. L. & Fujii, T. (1993). Petrologic and sulfur isotopic significance of highly oxidized and sulfur-rich magma of Mt. Pinatubo, Philippines. *Geology* **21,** 699–702.

Imai, A., Listanco, E. L. & Fujii, T. (1996). Highly oxidized and sulfur-rich dacitic magma of Mount Pinatubo: implication for metallogenesis of porphyry copper mineralization in the Western Luzon arc. In: Newhall, C. G. & Punongbayan, R. S. (eds) *Fire and Mud. Eruptions and Lahars of Mount Pinatubo, Philippines*. Seattle: University of Washington Press, pp. 865–874.

Johnson, M. C. & Rutherford, M. J. (1989). Experimentally determined conditions in the Fish Canyon Tuff, Colorado, magma chamber. *Journal of Petrology* **30,** 711–737.

Kress, V. (1997). Magma mixing as a source for Pinatubo sulfur. *Nature* **389,** 591–593.

Luhr, J. F. (1990). Experimental phase relations of water- and sulfur-saturated arc magmas and the 1982 eruptions of El Chichòn volcano. *Journal of Petrology* **31,** 1071–1114.

Luhr, J. F. (1991). Volcanic shade causes cooling. *Nature* **354,** 104–103.

Luhr, J. F. & Melson, W. G. (1996). Mineral and glass compositions in June 15, 1991, pumices: evidence for dynamic disequilibrium in the Pinatubo dacite. In: Newhall, C. G. & Punongbayan, R. S. (eds) *Fire and Mud. Eruptions and Lahars of Mount Pinatubo, Philippines*. Seattle: University of Washington Press, pp. 733–750.

Luhr, J. F., Carmichael, I. S. E. & Varekamp, J. C. (1984). The 1982 eruptions of El Chichòn Volcano, Chiapas, Mexico: mineralogy and petrology of the anhydrite-bearing pumices. *Journal of Volcanology and Geothermal Research* **23,** 69–108.

Martel, C. (1996). Conditions pré-éruptives et dégazage des magmas andésitiques de la Montagne Pelée (Martinique): étude pétrologique et expérimentale. Ph.D. Thesis, Université d'Orléans, 200 pp.

Martel, C., Pichavant, M., Bourdier, J. L., Traineau, H., Holtz, F. & Scaillet, B. (1998). Magma storage conditions and control of eruption regime in silicic volcanoes: experimental evidence from Mt. Pelée. *Earth and Planetary Science Letters* **156,** 89–99.

Matthews, S. J., Jones, A. P. & Beard, A. D. (1994). Buffering of melt oxygen fugacity by sulphur redox reactions in calc-alkaline magmas. *Journal of Geological Society, London* **151,** 815–823.

Merzbacher, C. & Eggler, D. H. (1984). A magmatic geohygrometer: application to Mount St. Helens and other dacitic magmas. *Geology* **12,** 587–590.

Mori, J., Eberhart-Philips, D. & Harlow, D. (1996). Three dimensional velocity structure at Mount Pinatubo, Philippines: resolving magma bodies and earthquake hypocenters. In: Newhall, C. G. & Punongbayan, R. S. (eds) *Fire and Mud. Eruptions and Lahars of Mount Pinatubo, Philippines*. Seattle: University of Washington Press, pp. 371–382.

Nicholls, I. A., Oba, T. & Conrad, W. K. (1992). The nature of primary rhyolitic magmas involved in crustal evolution: evidence from an experimental study of cummingtonite-bearing rhyolites, Taupo volcanic zone, New Zealand. *Geochimica et Cosmochimica Acta* **56,** 955–962.

Pallister, J. S., Hoblitt, R. P. & Reyes, A. G. (1992). A basalt trigger for the 1991 eruptions of Pinatubo volcano? *Nature* **356,** 426–428.

Pallister, J. S., Hoblitt, R. P., Meeker, G. P., Newhall, C. G., Knight, R. J. & Siems, D. F. (1996). Magma mixing at Mount Pinatubo volcano: petrographical and chemical evidence from the 1991 deposits. In: Newhall, C. G. & Punongbayan, R. S. (eds) *Fire and Mud. Eruptions and Lahars of Mount Pinatubo, Philippines*. Seattle: University of Washington Press, pp. 687–732.

Pasteris, J. D., Wopenka, B., Wang, A. & Harris, T. N. (1996). Relative timing of fluid and anhydrite saturation: another consideration in the sulfur budget of the Mount Pinatubo eruption. In: Newhall, C. G. & Punongbayan, R. S. (eds) *Fire and Mud. Eruptions and Lahars of Mount Pinatubo, Philippines*. Seattle: University of Washington Press, pp. 875–891.

Pichavant, M. (1987). Effects of B and H_2O on liquidus phase relations in the haplogranite system at 1 kbar. *American Mineralogist* **72,** 1056–1070.

Pownceby, M. I. & O'Neill, H. St. C. (1994). Thermodynamic data from redox reactions at high temperatures. III. Activity–composition relations in Ni–Pd alloys from EMF measurements at 850–1250 K, and calibration of the NiO + Ni–Pd assemblage as a redox sensor. *Contributions to Mineralogy and Petrology* **116,** 327–339.

Robie, R. A., Hemingway, B. S. & Fisher, J. R. (1979). Thermodynamic properties of minerals and related substances at 298·15 K and 1 bar (10^5 pascals) pressure and at higher temperature. *US Geological Survey Bulletin* **1452**.

Roux, J. & Lefèvre, A. (1992). A fast quench device for internally heated pressure vessels. *European Journal of Mineralogy* **4,** 279–281.

Rutherford, M. J. & Devine, J. D. (1988). The May 1, 1980 eruption of Mount St. Helens: 3, Stability and chemistry of amphibole in the magma chamber. *Journal of Geophysical Research* **93,** 949–959.

Rutherford, M. J. & Devine, J. D. (1996). Pre-eruption pressure–temperature conditions and volatiles in the 1991 Mount Pinatubo magma. In: Newhall, C. G. & Punongbayan, R. S. (eds) *Fire and Mud. Eruptions and Lahars of Mount Pinatubo, Philippines*. Seattle: University of Washington Press, pp. 751–766.

Rutherford, M. J., Sigurdsson, H. & Carey, S. (1985). The May 1, 1980 eruption of Mount St. Helens: 1, Melt composition and experimental phase equilibria. *Journal of Geophysical Research* **90,** 2929–2947.

Sato, H. (1984). Partition relation of K between magma and plagioclase in a suite of volcanic rocks from northeast Shikoku, Japan. *Journal of Japanese Association of Mineralogy, Petrology and Economic Geology* **79,** 47–59.

Scaillet, B., Pichavant, M., Roux, J., Humbert, G. & Lefèvre, A. (1992). Improvements of the Shaw membrane technique for measurement and control of f_{H_2} at high temperatures and pressures. *American Mineralogist* **77,** 647–655.

Scaillet, B., Pichavant, M. & Roux, J. (1995). Experimental crystallization of leucogranite magmas. *Journal of Petrology* **36,** 663–705.

Schmidt, M. S. (1992). Amphibole composition in tonalite as a function of pressure: an experimental calibration of the Al-in-hornblende barometer. *Contributions to Mineralogy and Petrology* **110,** 304–310.

Schmidt, B. C., Scaillet, B. & Holtz, F. (1995). Accurate control of fH_2 in cold seal pressure vessels with the Shaw membrane technique. *European Journal of Mineralogy* **7,** 893–903.

Shaw, H. R. & Wones, D. R. (1963). Fugacity coefficients for hydrogen gas between 0° and 1000°C, for pressures to 3000 atm. *American Journal of Science* **262,** 918–929.

Silver, L. A., Ihinger, P. D. & Stolper, E. (1990). The influence of bulk composition on the speciation of water in silicate glasses. *Contributions to Mineralogy and Petrology* **104,** 142–162.

Sisson, T. W. & Grove, T. L. (1993). Experimental investigations of the role of H_2O in calc-alkaline differentiation and subduction zone magmatism. *Contributions to Mineralogy and Petrology* **113,** 143–166.

Stormer, J. C. (1983). The effects of recalculation on estimates of temperature and oxygen fugacity from analyses of multi-component iron–titanium oxides. *American Mineralogist* **68,** 586–594.

Tait, S., Jaupart, C. & Vergniolle, S. (1989). Pressure, gas content and eruption periodicity of a shallow, crystallizing magma chamber. *Earth and Planetary Science Letters* **92,** 107–123.

Taylor, J. R., Wall, V. J. & Pownceby, M. I. (1992). The calibration and application of accurate redox sensors. *American Mineralogist* **77,** 284–295.

Wallace, P. J. & Gerlach, T. M. (1994). Magmatic vapor source for sulfur dioxide released during volcanic eruptions: evidence from Mount Pinatubo. *Science* **265,** 497–499.

Wallace, P. J., Anderson, A. T. & Davis, A. M. (1995). Quantification of pre-eruptive exsolved gas contents in silicic magmas. *Nature* **377,** 612–615.

Webster, J. D., Holloway, J. R. & Hervig, R. L. (1987). Phase equilibria of a Be, U and F-enriched vitrophyre from Spor Mountain, Utah. *Geochimica and Cosmochimica Acta* **51,** 389–402.

Westrich, H. R. & Gerlach, T. M. (1992). Magmatic gas source for the stratospheric SO_2 cloud from the June 15, 1991 eruption of Mount Pinatubo. *Geology* **20,** 867–870.

Whitney, J. A. (1972). The effect of reduced H_2O fugacity on the buffering of oxygen fugacity in hydrothermal experiments. *American Mineralogist* **57,** 1902–1908.